

RESEARCH ARTICLE

Syntaxin 7 contributes to breast cancer cell invasion by promoting invadopodia formation

Sameena Parveen¹, Amrita Khamari¹, Jyothikamala Raju², Marc G. Coppelino³ and Sunando Datta^{1,*}

ABSTRACT

Invasion in various cancer cells requires coordinated delivery of signaling proteins, adhesion proteins, actin-remodeling proteins and proteases to matrix-degrading structures called invadopodia. Vesicular trafficking involving SNAREs plays a crucial role in the delivery of cargo to the target membrane. Screening of 13 SNAREs from the endocytic and recycling route using a gene silencing approach coupled with functional assays identified syntaxin 7 (STX7) as an important player in MDA-MB-231 cell invasion. Total internal reflection fluorescence microscopy (TIRF-M) studies revealed that STX7 resides near invadopodia and co-traffics with MT1-MMP (also known as MMP14), indicating a possible role for this SNARE in protease trafficking. STX7 depletion reduced the number of invadopodia and their associated degradative activity. Immunoprecipitation studies revealed that STX7 forms distinct SNARE complexes with VAMP2, VAMP3, VAMP7, STX4 and SNAP23. Depletion of VAMP2, VAMP3 or STX4 abrogated invadopodia formation, phenocopying what was seen upon lack of STX7. Whereas depletion of STX4 reduced MT1-MMP level at the cell surfaces, STX7 silencing significantly reduced the invadopodia-associated MT1-MMP pool and increased the non-invadosomal pool. This study highlights STX7 as a major contributor towards the invadopodia formation during cancer cell invasion.

This article has an associated First Person interview with the first author of the paper.

KEY WORDS: STX7, VAMP2, VAMP3, STX4, MT1-MMP, Tks5, Cortactin, Invadopodia, SNAREs

INTRODUCTION

Tumor cells acquire invasive capability upon sensing their extracellular milieu. Invasion involves alteration of cell-to-cell and cell–extracellular matrix (ECM) contact and remodeling of the surrounding matrix to form micro-tracks that can be used by other cells during metastasis (Friedl et al., 1997; Wolf et al., 2007; Kawauchi, 2012). ECM remodeling is achieved through the secretion of various matrix-degrading proteases, such as soluble matrix metalloproteinases (MMPs) and membrane-type MMPs. These proteases help cleave the surrounding matrix proteins, enabling pathways for the trailing cells (Stetler-Stevenson, 2001;

Chun et al., 2004; Even-Ram and Yamada, 2005; Wolf et al., 2007). Proteolytically active proteases with ECM degradation capability are accumulated and secreted from a specialized protrusive structures, formed at the ventral surface of the cells, termed invadopodia (Artym et al., 2006; Steffen et al., 2008; Poincloux et al., 2009; Kessenbrock et al., 2010; Frittoli et al., 2011; Itoh, 2015; Jacob and Prekeris, 2015; Linder, 2015; Castro-Castro et al., 2016; Cepeda et al., 2016; Jabłońska-Trypuć et al., 2016; Qiang et al., 2019). Invadopodium formation is a tightly regulated process involving initiation, assembly and maturation (Murphy and Courtneidge, 2011). Localized delivery of proteases to the invadopodia requires various intracellular trafficking machinery (Steffen et al., 2008; Frittoli et al., 2014; Kajiho et al., 2016; Sharma et al., 2020). Vesicles of endomembrane origin exploit soluble N-ethylmaleimide-sensitive factor attachment protein receptors (SNAREs) to target and fuse to the plasma membrane (PM) (Bonifacino and Glick, 2004; Hong, 2005; Jahn and Scheller, 2006; Cai et al., 2007; Südhof and Rothman, 2009). Several studies have shown that SNAREs are involved in transport of MT1-MMP (also known as MMP14) to the cell surface (Miyata et al., 2004; Steffen et al., 2008; Kean et al., 2009; Williams et al., 2014; Clancy et al., 2015; Sneeggen et al., 2019; West et al., 2021) although the role of SNAREs in regulating the invadopodia number in cancer cells is yet to be investigated.

Combining a reverse genetics approach with microscopic and biochemical studies, here we aimed at identifying SNAREs of the endocytic and recycling pathways with potential roles in invadopodia-mediated breast cancer cell invasion. The current study demonstrates that STX7 is crucial for the formation of invadopodia and the associated gelatin degradation and invasion activity. STX7 interacts with multiple SNARE proteins, forming multiple SNARE complexes. Depletion of these interacting partners phenocopies the effects of STX7 depletion.

RESULTS

STX7 contributes to efficient ECM degradation and Matrigel invasion

To investigate the role of SNAREs in matrix remodeling and invasion, 13 SNAREs of the endocytic and recycling pathway were screened using a SMART pool siRNA-based reverse genetics approach. Depletion of six of 13 SNAREs (Fig. S1A) led to significant reduction in gelatin degradation activity in MDA-MB-231 cells (Fig. 1A; Fig. S1B). Subsequently, an Matrigel invasion assay showed a significant reduction in invasive potential upon depletion of STX2, STX4, STX7, VAMP3 and VAMP7 (Fig. 1B; Fig. S1C).

Previously, STX2 was found to be involved in invasion and metastasis by activating MMP-9 expression in hepatocellular carcinoma (Jia et al., 2011). Similarly, STX4, VAMP3 and VAMP7 are known to regulate MT1-MMP trafficking during invasion (Steffen et al., 2008; Kean et al., 2009; Williams et al., 2014; Brasher et al., 2017). Although the role of STX7 in endosome maturation (Mullock et al., 2000; Nakamura et al., 2000; Ward et al., 2000) is well known,

¹Department of Biological Sciences, Indian Institute of Science Education and Research, Bhopal, Bhopal 462066, India. ²Thazhathemalayil House, Thodupuzha East PO, Keerikode, Kerala 685585, India. ³Department of Molecular and Cellular Biology, University of Guelph, Ontario N1G 2W1, Canada.

*Author for correspondence (sunando@iiserb.ac.in)

DOI: 10.1242/jcs.259576. S.P., 0000-0002-9181-8283; A.K., 0000-0003-3454-2759; J.R., 0000-0001-9444-6211; M.G.C., 0000-0002-4538-7929; S.D., 0000-0002-1417-0276

Handling Editor: Andrew Ewald

Received 12 November 2021; Accepted 12 May 2022

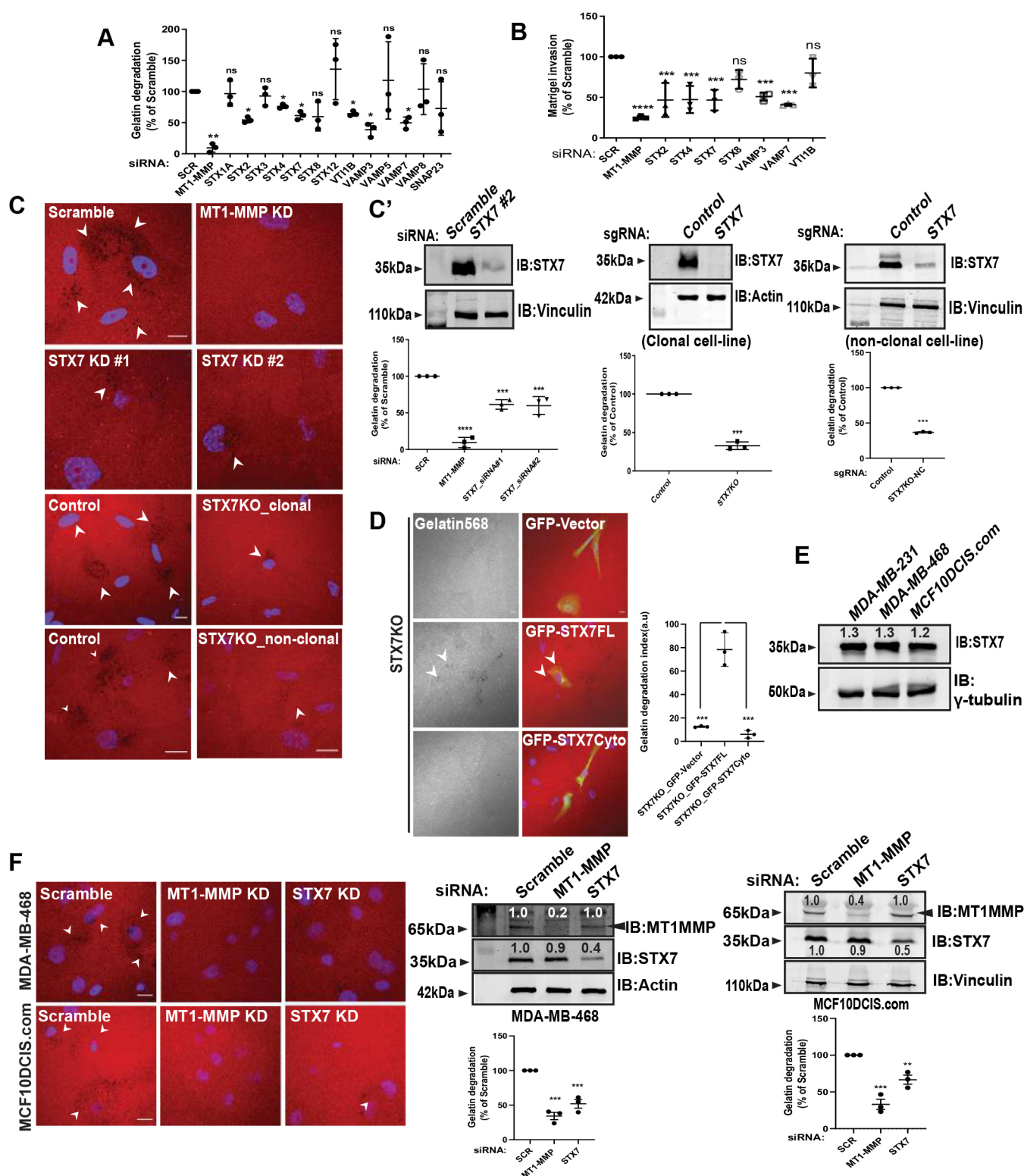


Fig. 1. See next page for legend.

its contribution to cancer cell invasion is unexplored. Therefore, we focused on STX7 in the current study.

To exclude off-target effects, an alternative siRNA (siRNA #2) was used, and a CRISPR-Cas9-mediated STX7 knockout clonal (STX7KO) as well as a non-clonal (STX7KO-NC) cell line was established (Fig. 1C'; Fig. S1D). Silencing of STX7 abrogated gelatin degradation (Fig. 1C). A similar phenotype was observed for cells with

reduced expression of MT1-MMP (Fig. 1C). The loss of ECM degradation in STX7KO cells could be rescued by overexpressing wild-type GFP-STX7 (STX7FL), although the trans-membrane deleted mutant (STX7Cyto) failed to do so (Fig. 1D). The level of expression of the exogenous STX7 (GFP-STX7) was found to be 1.0 ± 0.1 , which was comparable to the endogenous STX7 with expression of 1.1 ± 0.0 (mean \pm s.d., arbitrary units; Fig. S1E,E').

Fig. 1. STX7 acts as an efficient ECM degradation and remodeling machinery. (A) MDA-MB-231 cells were transfected with the indicated siRNA. SCR, scrambled siRNA. At 60 h post transfection, cells were seeded on Alexa Fluor 568-labeled gelatin-coated coverslip for 12 h. Images were acquired randomly, and degradation activity was quantified and plotted ($N=3$, $n\geq 300$). $^{*}P<0.05$; $^{**}P<0.01$; ns, not significant (one-way ANOVA with Dunnett's multiple comparisons test). (B) MDA-MB-231 cells were depleted for the indicated molecules, seeded on Matrigel-coated cell inserts and allowed to invade for 20 h. Invasive cells were counted, and the percentage of invaded cells was plotted ($N=3$). $^{***}P<0.001$; $^{****}P<0.0001$; ns, not significant (one-way ANOVA with Dunnett's multiple comparisons test). (C,C') The KD efficiency of STX7 in MDA-MB-231 cells using siRNA or sgRNA was confirmed by western blotting. Subsequently, a gelatin degradation assay was performed using MT1-MMP, and STX7 depleted or STX7 silenced clonal (STX7KO) and non-clonal (STX7KO-NC) cells. Images were acquired randomly, and degradation activity was quantified and plotted. Arrowheads represent degradation spots ($N=3$, $n\geq 300$). $^{***}P<0.001$, $^{****}P<0.0001$ [one-way ANOVA with Dunnett's multiple comparisons test (left) or paired two-tailed Student's *t*-test (middle and right)]. (D) MDA-MB-231 STX7KO cells were transfected with GFP-Vector, GFP-STX7FL or GFP-STX7Cyto and used for the gelatin degradation assay as described above. Arrowheads represent degradation spots ($N=3$, $n\geq 300$). $^{***}P<0.001$ (one-way ANOVA with Tukey's multiple comparisons test). a.u., arbitrary units. (E) For comparative analysis of STX7 expression, the indicated cell lines were lysed and immunoblotted using anti-STX7 and anti- γ -tubulin antibodies (loading control). Numbers over the blots represent the band quantification for the blot shown, which represents one of three experimental repeats. (F) MDA-MB-468 and MCF10DCIS.com cells were treated with siRNA for STX7 and MT1-MMP. The efficiency of gene silencing was detected by immunoblotting using anti-STX7 and anti-MT1-MMP antibodies (highlighted by black arrowheads); actin and vinculin were used as loading controls, respectively. Numbers over the blots represent the band quantification for the blots shown. Subsequently, gelatin degradation assay was performed as above. Arrowheads indicate the degradation spot ($N=3$, $n\geq 300$). $^{**}P<0.01$, $^{***}P<0.001$ (one-way ANOVA with Dunnett's multiple comparisons test). *N*, number of experimental repeats; *n*, number of cells analyzed. All the graphs represent means \pm s.d. Scale bars: 10 μ m.

Expression of the other SNAREs identified from the initial screen in STX7-depleted cells was unaltered under these conditions indicating that the observed phenotype is specific to STX7 (Fig. S1F).

To establish that the involvement of STX7 is not limited to MDA-MB-231 cells, we extended the study to MDA-MB-468 and MCF10DCIS.com cell lines. Immunoblot analysis revealed a similar expression profile for STX7 in both the cell lines to that in MDA-MB-231 cells (Fig. 1E). STX7 depletion led to a significant loss in ECM degradation for both the cell lines, as revealed by gelatin degradation assay (Fig. 1F). Together, these observations implicate the involvement of STX7 in breast cancer cell invasion.

STX7 resides on endosomal membrane and co-traffics to the invadopodia with MT1-MMP

To further understand the role of STX7, we studied its subcellular localization in MDA-MB-231 cells. STX7 was observed to colocalize with EEA1 (45.0 \pm 4.0%), Rab11 (31.0 \pm 3.2%), Rab4 (28.0 \pm 2.6%), and CD63 (15.0 \pm 3.9%) (mean \pm s.d., Fig. S1G,G'). Next, we sought to investigate the association of STX7 with invadopodia. We observed (1) several STX7- and Tks5 (an invadopodium marker, also known as SH3PXD2A; Murphy and Courtneidge, 2011; Zagryazhskaya-Masson et al., 2020)-positive puncta in close vicinity, as revealed by total internal reflection fluorescence microscopy (TIRF-M) (Fig. 2A), (2) STX7 near sites of gelatin degradation along with Tks5 (Fig. 2B), and (3) STX7 puncta positive for Tks5 and F-actin (Fig. 2C). Similarly, STX7 was observed to be associated with another invadopodium marker, cortactin (Mader et al., 2011; Beaty et al., 2013; Hayes et al., 2013). That is, (1) several GFP-STX7 puncta were positive for cortactin and F-actin (Fig. S2A), and (2) STX7 was

observed near sites of gelatin degradation along with cortactin (Fig. S2B). These observations suggest that STX7 is associated with endosomes and invadopodia.

Next, we investigated the effect of STX7 overexpression on invadopodium formation. It was observed that, compared to GFP-Vector, the overexpression of STX7 (GFP-STX7) did not stimulate invadopodia formation (Fig. S2C). However, the overexpression of STX7 did promote/increase STX7 colocalization with Tks5 in invadopodia (Fig. S2D) perhaps explaining the positive effect of enhanced gelatin degradation upon GFP-STX7 overexpression (Fig. 1D). Furthermore, to understand whether STX7 overexpression changes its localization, we compared the distribution of endogenous STX7 with that of EEA1 in the presence of GFP-STX7 by immunofluorescence. The percentage overlap of GFP-STX7 with STX7 and EEA1 was observed to be 56.0 \pm 6.4% and 52.4 \pm 9.3%, respectively (mean \pm s.d.; Fig. S2E). The localization of STX7 with EEA1 in the presence of GFP-STX7 was found to be 46.0 \pm 4.0% (Fig. S2E), which is similar to that found in the untreated condition (45.0 \pm 4.0%) (Fig. S1G'). Therefore, STX7 overexpression does not have any effect on its localization (Fig. S2E).

Remodeling of ECM requires targeted delivery of proteases to the invadosomes. Immunostaining revealed that 30.0 \pm 3.0% of vesicles positive for STX7 are positive for MT1-MMP and EEA1, whereas only 16.8 \pm 1.9% of vesicles positive for STX7 are positive for MT1-MMP and CD63 (mean \pm s.d.; Fig. 2D). Confocal and TIRF-based live-cell microscopy revealed that GFP-STX7 and Cherry-MT1-MMP co-traffic intracellularly and near the PM (Fig. 2E,F; Movies 1, 2). Thus, our data suggest that STX7 might be involved in the delivery of MT1-MMP to the cell surface from endosomes. This observation is in concurrence with earlier reports from multiple cell lines showing that STX7 undergoes recycling between endosomes and the PM (Heng Wong et al., 1998; Prekeris et al., 1999; Kasai and Akagawa, 2001; Bilan et al., 2008; Feldmann et al., 2009).

STX7 depletion leads to reduced invadopodia formation and associated ECM degradation

Since STX7 and MT1-MMP co-traffic to the PM, we hypothesized that STX7 depletion would impede MT1-MMP delivery. Surprisingly, TIRF-M imaging in STX7KO cells expressing pHluorinMT1-MMP (pHMT1-MMP) revealed a significant increase in the number of MT1-MMP vesicles near the PM (Fig. 3A). However, STX4 gene depletion, as expected, caused reduced protease delivery to the surface (Fig. 3A,A'; Movies 3, 4). We quantified the surface MT1-MMP level through biotinylation experiments and found a significant increase in the PM pool compared to the control, whereas levels of endogenous MT1-MMP remained unaltered in the STX7 KD cells (Fig. 3B). Surface biotinylated β 1-integrin and EGFR levels remained unaltered (Fig. 3B). Next, we carried out an anti-MT1-MMP antibody uptake assay (Remacle et al., 2003) in STX7KO cells and observed significantly increased uptake of the antibodies, consistent with increased MT1-MMP availability at the PM (Fig. 3C). The above findings demonstrate that silencing of STX7 results in significantly higher MT1-MMP levels at the PM. To rule out the possibility that STX7 perturbation is altering endocytic pathways in the MDA-MB-231 cells, MT1-MMP and transferrin (Tfn) uptake were measured. There was no effect observed on the endocytosis of MT1-MMP or Tfn, as measured by percentage of endocytosed MT1-MMP (Fig. 3D) or internalized Tfn (Fig. S3A). However, compared to control cells, the increased intensity of accumulated Tfn at the end of 60-min of chase suggested that STX7 is involved in recycling of this cargo (Fig. S3B).

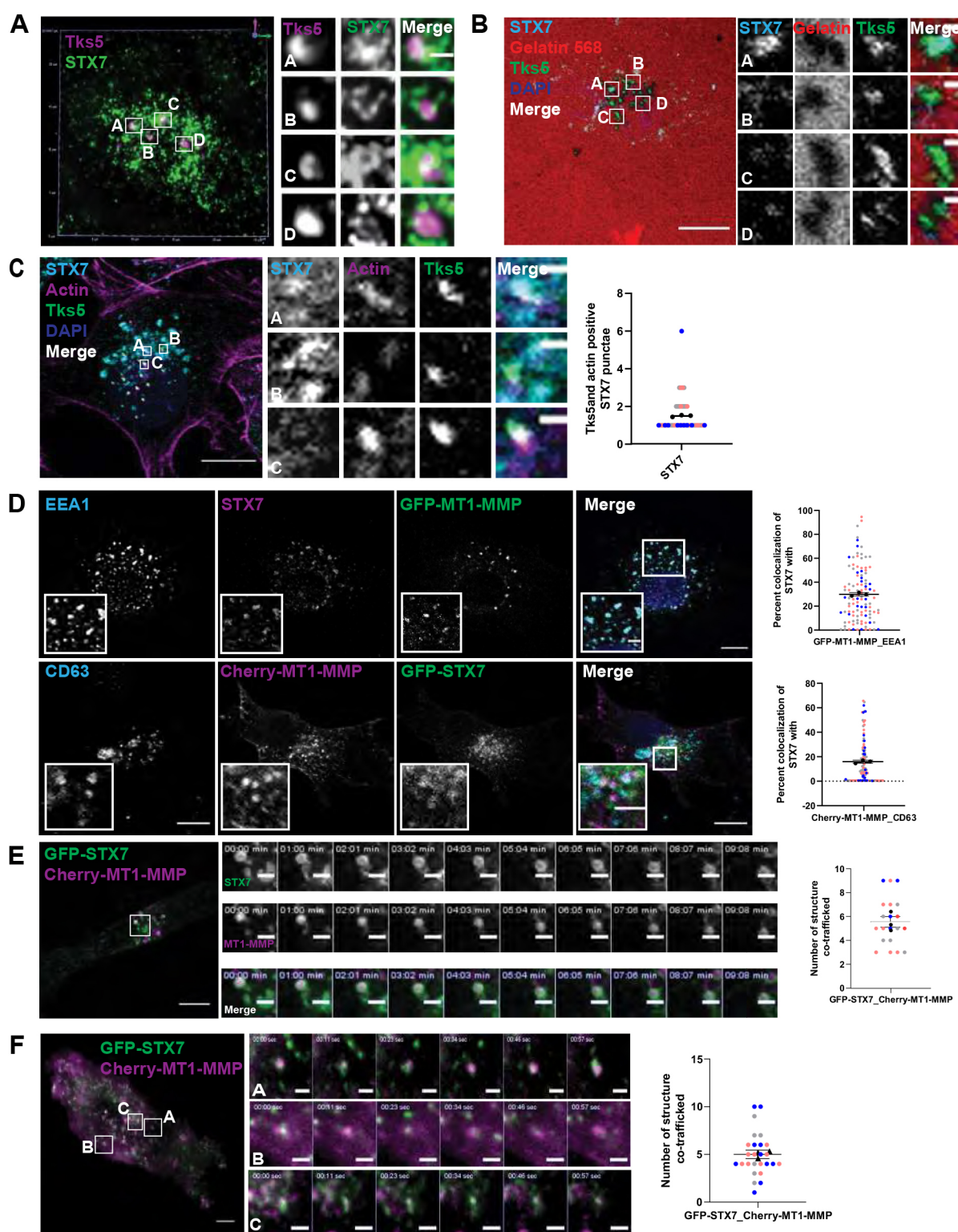


Fig. 2. See next page for legend.

We also used a dominant-negative form of STX7 to study its role in MT1-MMP delivery. The overexpression of STX7^{Cyto} reduced MT1-MMP antibody uptake (Fig. S3C) and surface MT1-MMP level (Fig. S3D), as revealed by confocal and TIRF microscopy, respectively. The opposing effect of STX7 depletion versus overexpression of STX7^{Cyto} on MT1-MMP levels at the PM is possibly due to the dominant-negative effect caused

by the mutant. The ability of the mutant to bind to its cognate SNAREs leading to the formation of inactive complexes might be a possible reason for the observed disparity (Suzuki et al., 2003).

The contrasting outcomes of higher protease delivery to the surface (Fig. 3A–C) but a reduced invadopodia-associated protease activity (Fig. 1A–C) prompted us to measure the availability of

Fig. 2. Endosomal STX7 recycles to invadopodia for the fusion activity. (A) MDA-MB-231 cells were immunostained for STX7 and Tks5. Deconvoluted TIRF images are shown. Boxed regions are shown in an enlarged view on the right, and represent the multiple occurrences of STX7–Tks5 being present at the TIRF surface ($N=2$, $n=30$). Scale bar: 3 μm (in magnified views). (B) MDA-MB-231 cells were plated over Alexa Fluor 568-labeled gelatin-coated coverslip and immunostained for STX7 and Tks5 followed by DAPI staining. Boxed regions are shown in an enlarged view on the right, and show STX7 and Tks5 puncta localization near a labeled gelatin degradation area ($N=2$, $n=50$). Scale bars: 10 μm (main image), 1 μm (magnified box). (C) MDA-MB-231 cells were plated over gelatin-coated coverslip and immunostained for STX7 and Tks5 followed by labeling with Phalloidin-568 (F-actin) and DAPI. Boxed regions are shown in an enlarged view on the right, and show STX7 puncta positive for Tks5–actin. Graph shows Tks5- and actin- positive STX7 puncta numbers per cell ($N=3$, $n=43$). Scale bars: 10 μm (main image), 1 μm (magnified box). (D) Upper panel, GFP-MT1-MMP transfected MDA-MB-231 cells were immunostained for STX7 and EEA1 followed by DAPI staining. Inset represents zoomed-in view of the boxed region ($N=3$, $n=79$). Lower panel, GFP-STX7 and Cherry-MT1-MMP transfected MDA-MB-231 cells were immunostained for CD63 followed by DAPI staining. Inset represents zoomed-in view of the boxed region ($N=3$, $n=92$). Scale bars: 10 μm (main images), 3 μm (insets). The percentage colocalization of STX7 with MT1-MMP and EEA1 or CD63 was quantified and plotted. (E) MDA-MB-231 cells with co-expression of GFP-STX7 and Cherry-MT1-MMP were subjected to live-cell imaging. An enlarged view of the boxed region is shown on the right, representing the co-trafficking of the molecules over time. Graph represents the co-transport of GFP-STX7 and Cherry-MT1-MMP ($N=3$, $n=20$). Scale bars: 10 μm (main images), 3 μm (magnified box). (F) MDA-MB-231 cells with co-expression of GFP-STX7 and Cherry-MT1-MMP were subjected to live-cell TIRF imaging. An enlarged view of the boxed region represents the trafficking of both the molecules at the surface. Graph represents the co-transport of GFP-STX7 and Cherry-MT1-MMP ($N=3$, $n=26$). Scale bars: 10 μm (main images), 3 μm (magnified box). For data that are displayed using SuperPlots, each biological replicate is distinctly color-coded and each dot represents percentage colocalization for identified multicolor objects or number of identified multicolor objects in a field of view (frame), as described in the Materials and Methods. N , number of experimental repeats; n , number of cells analyzed. All the graph represents means \pm s.d.

MT1-MMP at the invadopodia. Results from TIRF-M showed that in MDA-MB-231 STX7KO cells there was reduced numbers of Tks5-positive MT1-MMP puncta at the surface compared to the control. However, Tks5-negative MT1-MMP puncta were abundant at the TIRF plane (Fig. 4A), thus corroborating our above observations (Fig. 3A–C). This prompted us to investigate whether reduced MT1-MMP availability at the invadopodia is due to mis-trafficking or reduced invadopodia formation itself. MDA-MB-231 STX7KO and STX7KO-NC cells immunostained for the invadopodia markers Tks5 and cortactin (Fig. 4B) showed reduced invadopodia formation under TIRF-M. Reduction in invadopodia formation was further confirmed by examination of Tks5 and F-actin in STX7KO cells (Fig. 4C). Similar observations showing reduced invadopodia formation and fewer MT1-MMP-positive invadosomes were obtained with confocal microscopy (Fig. 4D). Several reports have demonstrated the role of cortactin phosphorylation in promoting invadopodia formation or degradation depending upon the phosphorylated residue (Sangrar et al., 2007; Ayala et al., 2008; Mader et al., 2011; Mukherjee et al., 2012; Zhao et al., 2012; Beatty et al., 2013; Hayes et al., 2013; Rosenberg et al., 2017). We measured the level of tyrosine-phosphorylated cortactin (phospho-cortactin) and found it to be slightly higher in the STX7KO cells (Fig. 4E).

Overall, we conclude that the depletion of STX7 results in targeting more MT1-MMP vesicles to the surface but reduces invadopodia formation, leading to compromised ECM degradation and Matrigel invasion.

STX7 forms multiple SNARE complexes with endosomal SNAREs, contributing to the invadopodia-associated activity

STX7 mediates homotypic fusion of late endosomes (LEs) and heterotypic fusion of LE–lysosomes by forming trans-SNARE complexes consisting of STX7–STX8–Vti1b–VAMP7 or STX7–STX8–Vti1b–VAMP8, respectively (Pryor et al., 2004; Achuthan et al., 2008). Here, we sought to identify cognate SNARE partner(s) of STX7 that might be involved in fusion of MT1-MMP vesicles at invadopodia. We analyzed the endosomal and PM-residing SNAREs VAMP2, VAMP3, VAMP7, STX2, STX4 and SNAP23, which have been shown to have roles in ECM degradation either from our screen (Fig. 1A) or as reported previously (Miyagawa et al., 2019). A modified nanobody-based pulldown approach was employed (Rothbauer et al., 2006, 2008; Tang et al., 2013). GFP–SNAP23, GFP–VAMP2 and GFP–VAMP3 were able to pull down STX7 from cell lysates (Fig. 5A; Fig. S4A,B). The interaction of GFP–STX4 and GFP–VAMP7 with the STX7 was weak compared with the interaction seen for the other proteins (Fig. 5B; Fig. S4C,D). No interaction between endogenous STX2 and STX7 was detected (Fig. 5C). In concordance with these results, VAMP3 and VAMP7 have been previously shown to immunoprecipitate STX7 from HeLa cells and rat liver membrane (Pryor et al., 2004; Gordon et al., 2009).

Since STX7 interacted with multiple cognate SNARE partners, confocal microscopy was used to confirm the overlap of compartments containing endogenous STX7 and its partners in MDA-MB-231. STX7 colocalized abundantly with VAMP2 ($43.6\pm2.2\%$) followed by VAMP3 ($30.5\pm2.8\%$), VAMP7 ($22.0\pm3.7\%$), SNAP23 ($14.9\pm2.4\%$) and STX4 ($14.0\pm0.3\%$) (mean \pm s.d.; Fig. 5D,D'). Furthermore, the colocalization of STX7 was assessed with HA–VAMP3 and GFP–VAMP2, HA–VAMP3 and GFP–VAMP7, and HA–VAMP3 and GFP–STX4 to measure the overlap of STX7 with double-positive interacting partners (Fig. S4E,E'). TIRF-M live-cell imaging also revealed that these binding partners co-traffic to the cell surface (Movies 5–7).

Based on these observations, we hypothesized that a lack of the above interacting SNAREs might phenocopy what was seen with a lack of STX7 regarding invadopodia-associated activity in MDA-MB-231 cells. Among the SNAREs, SNAP23 and VAMP7 were previously reported to contribute to trafficking of MT1-MMP to invadopodia (Williams et al., 2014). Moreover, and consistent with earlier reports and our present study, STX4 also plays a role in MT1-MMP trafficking (Brasher et al., 2017; Fig. 3A). Here, we observed that depletion of VAMP2 (Fig. S4F) led to a significant reduction in gelatin degradation (Fig. 6A). Depletion of VAMP2, VAMP3 and STX4 (Fig. S4F; Fig. 3A') led to a significant reduction in invadopodia formation (Fig. 6B–D) in MDA-MB-231 cells. Moreover, STX4 depletion resulted in reduced numbers of MT1-MMP vesicles near the PM that contrasted to the STX7 phenotype, where a subtle but significant increase in the MT1-MMP vesicle numbers was observed (Fig. 3A). This prompted us to assess the effects of silencing both the SNAREs. Contrary to depletion of STX7, co-depletion of STX4 and STX7 resulted in a reduction of MT1-MMP numbers vesicles at the PM, similar to what was seen with STX4 depletion (Fig. 6E; Movie 8). These observations indicate that both SNAREs are important for invadopodia formation and function. STX4, however, appears to have a more generalized function for MT1-MMP trafficking to the cell surface, as it abruptly causes a reduction in surface localization. STX7, in contrast, has a more-specific role in delivery of the protease to invadopodia in support of their degradative activity.

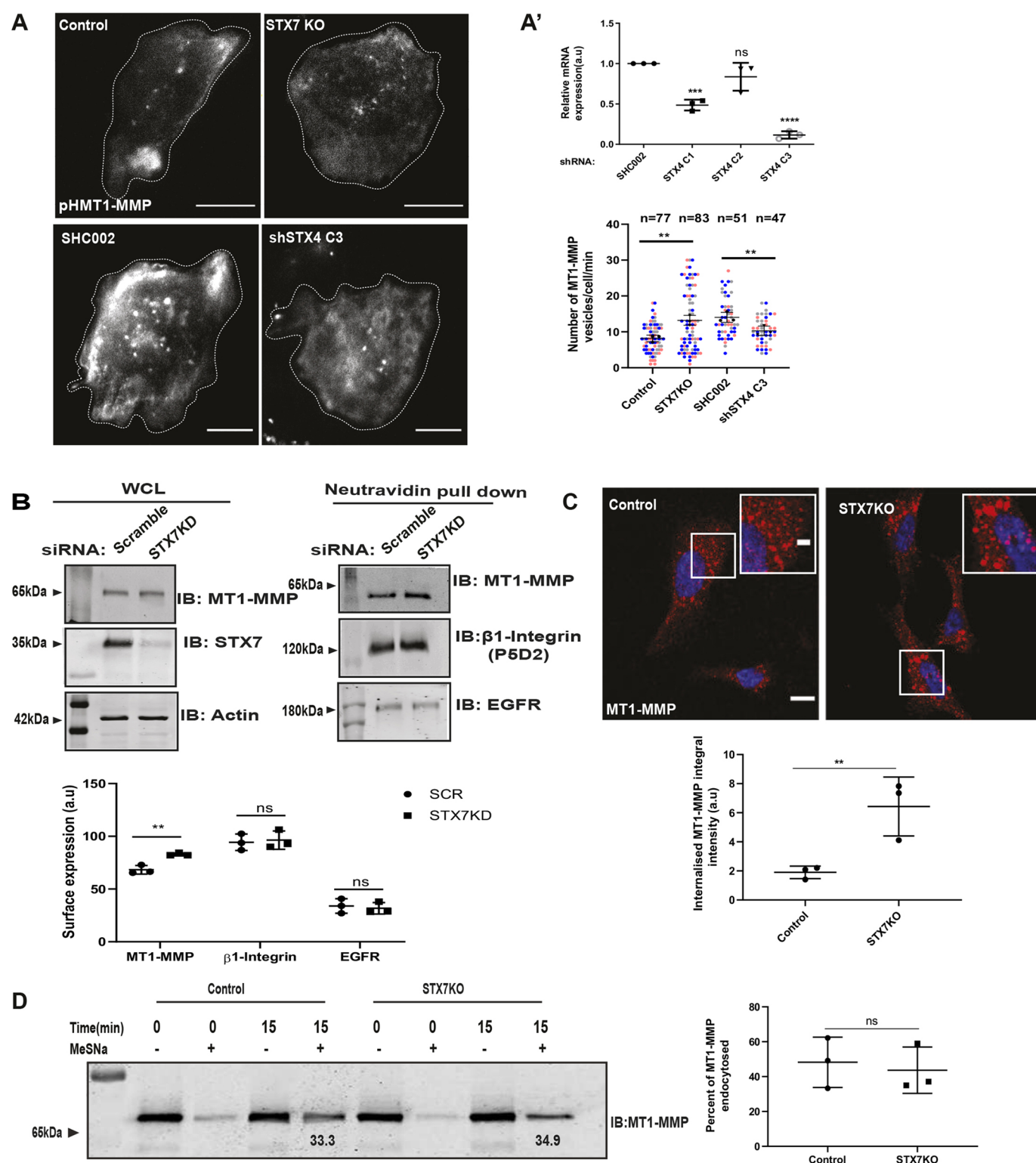


Fig. 3. See next page for legend.

DISCUSSION

The present study highlights that STX7 is crucial for invadopodia formation and associated activity. There could be several mechanisms by which STX7 contributes to this process. First, STX7 might be involved in the trafficking of signaling cargo crucial for the initiation stage of invadopodia formation (Mori et al., 2021; West et al., 2021). Integrins and EGFR have been shown to play an important role in this

stage (Destaing et al., 2010; Mader et al., 2011). However, we observed surface β 1-integrin and EGFR levels to be unaltered upon STX7 depletion (Fig. 3B). Second, there could be perturbed trafficking of MT1-MMP to the invadopodia. Previous reports indicate that invadopodia are formed at specialized domains of the PM containing cholesterol-rich lipid rafts. MT1-MMP has been observed to be enriched in lipid raft membrane fractions along with the other

Fig. 3. Loss of STX7 leads to enhanced MT1-MMP delivery to the PM.

(A) MDA-MB-231 control, SHC002 control (SHC002 is a control shRNA), STX7KO cells and STX4-depleted cells (shSTX4 C3) were transfected with pHMT1-MMP. Before the acquisition, cells were allowed to adhere to the gelatin-coated imaging dishes for 6 h and then subjected to TIRF-M. Dotted line highlights cell edge. Scale bars: 10 μ m. (A') The efficiency of gene silencing of STX4 was detected by qPCR ($N=3$). The number of MT1-MMP vesicles that are available in the TIRF plane and could form a track spanning over a minimum of four consecutive frames captured over 1 min duration was quantified and plotted [$N=3$, $n=77$ (control), $n=83$ (STX7KO), $n=51$ (SHC002), $n=47$ (shSTX4 C3)]. The data are displayed using SuperPlots, each biological replicate is distinctly color-coded. See Materials and Methods for details. $^{**}P<0.01$; $^{***}P<0.001$; ns, not significant (one-way ANOVA with Dunnett's multiple comparisons test). (B) Control and STX7KD MDA-MB-231 cells were subjected to biotinylation to measure the surface MT1-MMP, EGFR and β 1-integrin levels. Cells were labeled with non-cleavable biotin and lysed, followed by binding with Neutravidin beads. Protein bound beads were boiled using 2 \times SDS dye and separated on an SDS gel. The graph represents the densitometric analysis from the three individual blots for surface MT1-MMP level ($N=3$). $^{**}P<0.01$; ns, non-significant (unpaired two-tailed Student's *t*-test). WCL, whole-cell lysates. (C) MDA-MB-231 control and STX7KO cells were incubated with antibodies against MT1-MMP at 4°C for 1 h, then shifted to 37°C for 15 min. Cells were fixed, stained with DAPI, and imaged with a confocal microscope. The observed signal corresponds to internalized anti-MT1-MMP antibody ($N=3$, $n\geq 300$). The insets show the MT1-MMP antibody uptake by the cells. a.u., arbitrary units. $^{**}P<0.01$ (ratio paired two-tailed Student's *t*-test). Scale bar: 10 μ m (main image), 3 μ m (inset). (D) MDA-MB-231 control and STX7KO cells were incubated with cleavable biotin. Cells were treated with or without MeSNa at the 0 min time point (0 min + or 0 min –, respectively). Cells were then shifted to 37°C for 15 min to allow endocytosis and then reshifted to 4°C and treated with or without MeSNa (15 min + or 15 min –, respectively) to remove non-internalized biotin. Cells were lysed at indicated time points, followed by binding with Neutravidin beads. Protein-bound beads were boiled using 2 \times SDS dye and separated on an SDS gel. Immunoblotting was performed, and the level of MT1-MMP intensity was quantified by densitometric analysis of western blots. At 15 min time point, band intensity of 15 min +MeSNa was normalized to 15 min –MeSNa to measure the endocytosed population. The numbers on the blot represent quantification of the blot shown. See Materials and Methods for details. ns, non significant (ratio paired two-tailed Student's *t*-test). *N*, number of experimental repeats; *n*, number of cells analyzed. All the graph represents means \pm s.d.

invadopodia-associated proteins in MDA-MB-231 cells (Yamaguchi et al., 2009). It is possible that STX7 mediates specific delivery of MT1-MMP to lipid raft-enriched domains at the cell surface, initiating the assembly of a MT1-MMP–p130^{CAS}–SHIP2 complex at nascent invadopodia, preceding its expansion (Ferrari et al., 2019; Zagryazhskaya-Masson et al., 2020). This is impeded when STX7 is depleted, hence causing reduced invadopodia formation. Third, numerous studies have demonstrated that, although phosphorylation of cortactin on Tyr-421 and Tyr-466 by Src and Arg (also known as Abl2) is crucial for the invadopodia formation (Oser et al., 2009; Mader et al., 2011; Weidmann et al., 2016) and efficient ECM degradation (Clark et al., 2007; Ayala et al., 2008; Clark and Weaver, 2008), the phosphorylation of cortactin at Ser-405 and Ser-418 by ERK proteins leads to its E3 ubiquitin-ligase mediated degradation (Zhao et al., 2012). Hakai, an E3 ubiquitin-ligase, recognizes cortactin phosphorylated at Tyr-482. However, it still remains unclear whether Hakai targets proteasome-mediated cortactin degradation in cancer cells (Mukherjee et al., 2012; Jeannot and Besson, 2020). Our study suggests that STX7 silencing led to increased phospho-tyrosine cortactin levels (Fig. 4E), but decreased invadopodia formation (Fig. 4B,C), which might be explained by hyper-phosphorylation of Tyr-482 leading to its degradation and causing invadopodial disassembly. Fourth and finally, in an alternative hypothesis regarding the role of STX7 in invadopodia formation, a report suggests that, in comparison to soft

polyacrylamide gels, breast carcinoma cells cultured over hard polyacrylamide gels produce more invadopodia contributing to more ECM degradation (Alexander et al., 2008). This observation is further supported by a recent computational study demonstrating enhanced MT1-MMP secretion at invadopodia in stiff ECM (Kim et al., 2022). It was also found that, during membrane docking and fusion, the tension generated at the membrane due to the stiff ECM environment regulates the fusion pore dynamics and release of the vesicular content (Wang and Galli, 2018). It has been observed that substrate rigidity from 1.5 kPa to 28 kPa promotes the exocytosis of VAMP7 vesicles in fibroblasts, whereas VAMP2 exocytosis was insensitive to rigidity (Wang et al., 2018). Based on these studies, we hypothesize that increased matrix stiffness might trigger a mechanical response that allows STX7 to support transport of cargo molecules involved in initiation of invadopodia formation. The cargo molecules delivered to the surface initiate the formation of contact sites that contribute to MT1-MMP-dependent invadopodia formation (Zagryazhskaya-Masson et al., 2020). This can not be achieved when STX7-mediated cargo trafficking is impaired.

Our data also suggest that STX7 and its cognate partners VAMP2, VAMP3 or SNAP23, have stronger interaction than STX4 and VAMP7 (Fig. 5A,B; Fig. S4A–C). Of note, this is the first study to demonstrate the interaction between STX7 and VAMP2 or SNAP23 in a cellular context. VAMP3 depletion led to perturbed invadopodia formation (Fig. 5F) and cell invasion (Fig. 1B), consistent with previous studies showing the role of VAMP3 in MT1-MMP transport (Kean et al., 2009; Clancy et al., 2015; Sneeegen et al., 2019). We also observed the interaction of STX7 with VAMP3 in MDA-MB-231 cells, in agreement with a previous study performed in HeLa cells to investigate the trafficking of R-SNAREs (Gordon et al., 2009). Furthermore, VAMP2 has been reported as having a role in the fusion of recycling vesicles carrying Tfn–Tfn receptor (Kubo et al., 2015) and α 5 β 1 integrin (Hasan and Hu, 2010) to the PM, which is important for cell survival and migration in HeLa cells. Collectively, we propose that STX7 might be forming a functional SNARE complex with VAMP2 (Movie 5) or VAMP3 (Movie 6) that contributes to MT1-MMP-associated invadopodial activity. In contrast, STX4 exhibited weak interaction with STX7 and showed 15% colocalization. Accordingly, vesicles bearing both the SNAREs were also less abundant near the cell surface (Movie 7). Moreover, whereas STX4 depletion led to reduced MT1-MMP transport to the surface, the depletion of STX7 caused an enhanced MT1-MMP pool at the cell surface (Fig. 3A). Although depletion of both the molecules resulted in reduced invadopodia formation, and hence abrogated ECM degradation (Figs 5F and 1A), the role of these two SNAREs in MT1-MMP trafficking to cell surface appears to be distinct. The enhanced MT1-MMP trafficking upon STX7 silencing suggests a possible inhibitory role of STX7 in regulating the surface pool of the protease. Similar inhibitory role of t-SNAREs have been reported in an earlier study, where authors have demonstrated STX2 as an inhibitory SNARE in insulin granule secretion in pancreatic β -cells (Zhu et al., 2017).

Taken together, we conclude that STX7 forms multiple SNARE complexes by interacting with STX4, VAMP2, VAMP3 and VAMP7. Depletion of any of these SNAREs causes reduced invadopodia formation and breast cancer cell invasion (Fig. 7).

MATERIALS AND METHODS**Plasmids, antibodies and reagents**

The anti-rabbit EEA1 antibody was a kind gift from Professor Marino Zerial (Max Planck Institute of Molecular Cell Biology and Genetics, Dresden, Germany) and was used at 1:1000 [for immunofluorescence (IF)]. The following antibodies were purchased commercially: mouse anti-MT1-MMP

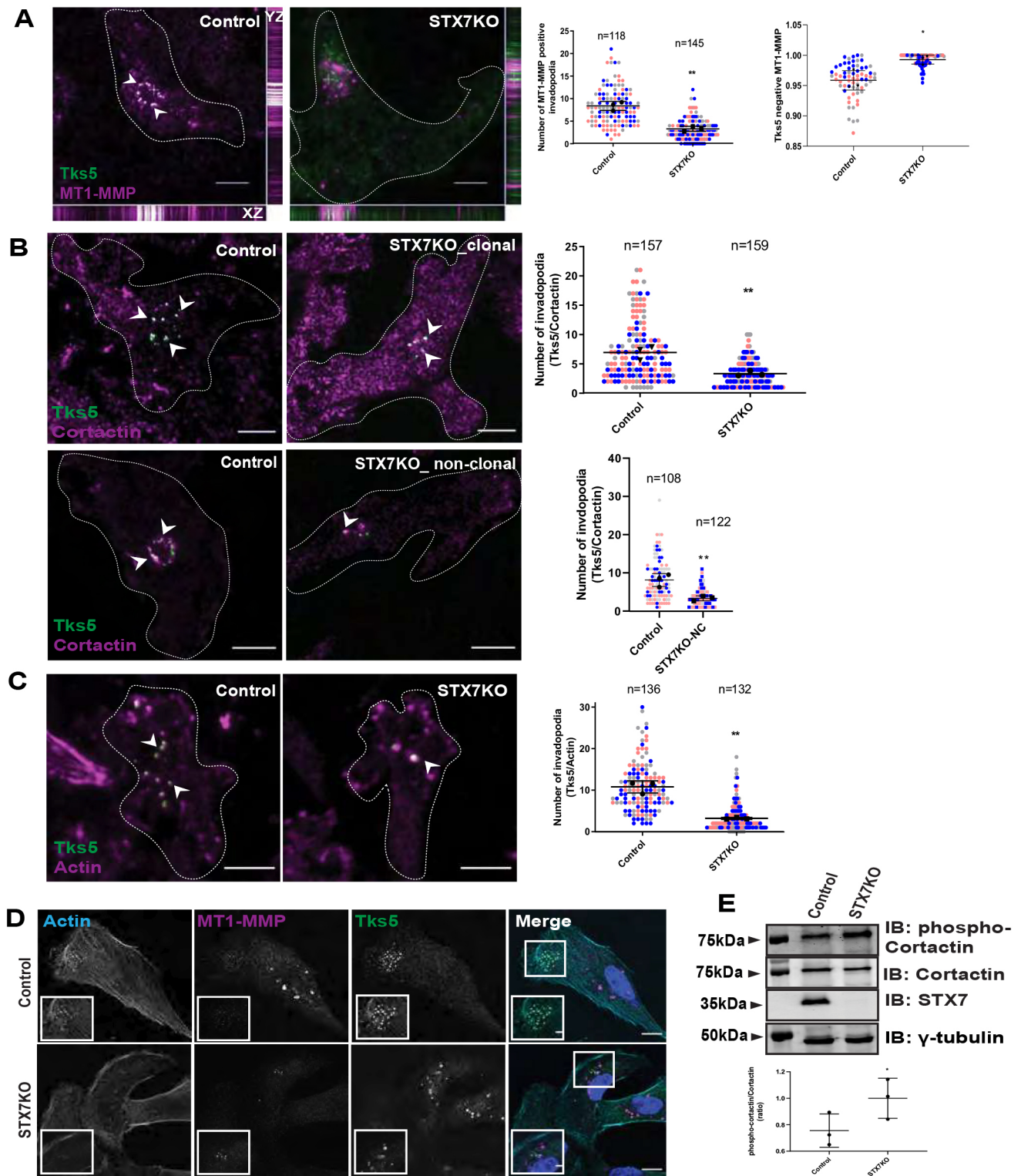


Fig. 4. See next page for legend.

(Millipore, MAB3328), 1:1000 [immunoblotting (IB)], 1:500 (IF); mouse anti-MT1-MMP (R& D Systems, MAB9181-SP), 1:200 (IF); mouse anti- α -tubulin (Sigma, V9131), 1:1000 (IB); mouse anti-cortactin (Millipore, 05-180), 1:1000 (IB), 1:300 (IF); mouse anti-transferrin receptor (Invitrogen, 136800), 1:500 (IF); rabbit anti-actin (Sigma, A2066), 1:2000 (IB); mouse anti-GFP (Roche, 11814460001), 1:2000 (IB); mouse anti- γ -tubulin (Sigma, T6557), 1:3000 (IB); mouse anti-CD63 (DSHB, H5C6), 1:500 (IF); rabbit anti-STX2 (Proteintech, 55033-1-AP), 1:1000 (IB), mouse

anti-STX7 (Santa Cruz Biotechnology, sc-514017), 1:1000 (IB), 1:300 (IF); mouse anti- β 1-integrin (P5D2, DSHB), 1:1000 (IB), mouse anti-phospho-tyrosine (Millipore, 05-1050), 1:1000 (IB); and rabbit anti-Tks5 (Santa Cruz Biotechnology, sc-30122), 1:500 (IF).

The pEGFPN1-STX7 (full length) and pmCherryN1-STX7 (full length) constructs were generated by amplifying STX7 from cDNA obtained from MDA-MB-231 cells with enzyme sites *SacI*/*SacII* using the following primers: Fwd, 5'-AAGAGCTCATGTCTTACACTCCAGGAGT-3' and

Fig. 4. Loss of STX7 leads to reduced invadopodia formation. (A) MDA-MB-231 control and STX7KO cells seeded on a gelatin-coated surface, were immunostained for MT1-MMP and Tks5. Cells were subjected to fixed cell TIRF imaging. Multiple z-stacks were acquired and best focused plane is represented as the XZ and YZ planes. Arrowheads represent colocalized puncta. The number of MT1-MMP puncta positive and negative for Tks5 (invadopodia) was counted and plotted [$N=3$, $n=118$ (control), $n=145$ (STX7KO)]. (B) MDA-MB-231 control, STX7KO and STX7KO-NC cells seeded on a gelatin-coated surface were immunostained for Tks5 and cortactin. Cells were subjected to fixed cell TIRF imaging. Arrowheads represent colocalized puncta. Invadopodia number was counted and plotted. For STX7KO cells, $N=3$, $n=157$ (control), $n=159$ (STX7KO); for STX7KO-NC cells, $N=3$, $n=108$ (control), $n=122$ (STX7KO-NC). (C) MDA-MB-231 control and STX7KO cells seeded on gelatin-coated surface, were immunostained for Tks5 and labeled for actin (Phalloidin-568). Cells were subjected to fixed cell TIRF imaging. Arrowhead represents colocalized puncta. Invadopodia number was counted and plotted. $N=3$, $n=136$ (control), $n=132$ (STX7KO). For A–C, dotted line highlights cell edge. Scale bars: 10 μm . $*P<0.05$, $**P<0.01$ (ratio paired two-tailed Student's *t*-test). (D) MDA-MB-231 control and STX7KO cells seeded on a gelatin-coated surface, immunostained for MT1-MMP and Tks5 followed by labeling with Phalloidin-647 and DAPI. Images were acquired using a confocal microscope. Inset represents a zoomed-in view of the boxed region ($N=3$, $n=50$). Scale bar: 10 μm (main image), 3 μm (inset). (E) MDA-MB-231 control and STX7KO cells were treated with pervanadate (40 μM) for 30 min. Subsequently, cells were lysed and proceeded for immunoblotting using anti-cortactin, anti-phosphotyrosine and anti-STX7 antibodies. Anti- γ -tubulin was used as a loading control. The level of phospho-cortactin was quantified and plotted. $*P<0.05$ (ratio paired two-tailed Student's *t*-test). For data that are displayed using SuperPlots, each biological replicate is distinctly color-coded and each dot represents identified multicolor objects in a field of view (frame), as described in the Material and Methods. All the graphs represent means \pm s.d. *N*, number of experimental repeats; *n*, number of cells analyzed.

Rev, 5'-ATCCGCGGGTGGTTCAATCCCCATA-3' and then cloning into pEGFPN1 and pmCherryN1 (kind gifts from Professor Marino Zerial, Max Planck Institute of Molecular Cell Biology and Genetics, Dresden, Germany). The Rat STX7cyto gene was amplified from pET28a-C(+) vectors (Professor Reinhard Jahn's laboratory, Max Planck Institute for Biophysical Chemistry, Göttingen, Germany) and cloned into pEGFPN1 and pmCherryN1 mammalian expression vectors with enzyme sites XhoI/HindIII using the following primers: Fwd, 5'-CTCGAGATGTCTTACAC-CTCCGGGGATT-3' and Rev, 5'-AAGCTTCTTTTCTGGATTGCGCT-GATAATTGCC-3'.

Cell culture and transient transfection

MDA-MB-231 and MDA-MB-468 cell lines were purchased from the ATCC and authenticated for contamination. Cells were maintained in L-15 (Invitrogen) medium with 10% fetal bovine serum (FBS), 100 $\mu\text{g ml}^{-1}$ penicillin, and 100 $\mu\text{g ml}^{-1}$ streptomycin (Invitrogen), hereafter L-15 complete medium, at 37°C in CO₂ free conditions. The MCF10DCIS.com cell line (kind gift from Professor Philippe Chavrier, Centre National de la Recherche Scientifique, Paris, France) was maintained in DMEM-F12 medium (Invitrogen) supplemented with 2 mM glutamine with 5% horse serum (Invitrogen) and maintained at 37°C in 5% CO₂ conditions. HeLa and HEK293T (ATCC) cells were cultured in Dulbecco's modified Eagle's medium (DMEM) with 10% FBS, 100 $\mu\text{g/ml}$ penicillin, 100 $\mu\text{g/ml}$ streptomycin and 2 mM glutamine (all from Invitrogen) at 37°C with 5% CO₂. For transient transfection of expression plasmids, cells were grown on coverslips in 24-well plates 1 day before the experiment. Cells were transfected at 50–60% confluency with 0.5 μg of plasmid DNA using LTX/Plus transfection reagent (Life Technologies).

siRNA and shRNA transfection

Cells were seeded 24 h before performing siRNA transfection. A standard protocol, available from Dharmacon, was used for transfection using Dharmafect as the transfection reagent. SMARTpool siRNAs targeting the gene of interest were purchased from Dharmacon. All siRNA were used at the working concentration of 10–20 nM. The sequences of SMARTpool

siRNAs are provided in Table S1. Cells were seeded 24 h before performing shRNA transfection. Plasmids for expression of shRNAs targeting the gene of interest were MISSION shRNA plasmids (Sigma). Cells were transfected at 50–60% confluency with 0.5 μg of plasmid DNA using LTX/Plus transfection reagent (Life Technologies). The sequences for MISSION plasmid shRNAs are provided in Table S2.

RNA extraction and quantitative real-time PCR

Total RNA was extracted from the cells using RNA easy kit (Qiagen, Cat. 74104), and cDNA was prepared using the High-Capacity RNA-to-cDNA kit (Life Technologies, Cat. 4387406). Real-time quantitative (q)PCR reactions were performed using the SYBR Green Kit and corresponding primers on Applied Biosystems 7300 real-time PCR system. Primer sequences are available upon request.

Immunofluorescence, microscopy and colocalization analysis

Cells were fixed in 4% paraformaldehyde (PFA) for 15 min at room temperature. Indirect immunofluorescence was performed on fixed cells permeabilized with 0.1% Triton X-100 for 10 min at room temperature, followed by blocking with 5% FBS in 1 \times PBS before staining with respective antibodies. The coverslips were mounted using Mowiol (Calbiochem, Cat. 475904) on glass slides and imaged using a Zeiss LSM 780 laser-scanning confocal microscope with the Zen 2010 software.

Data from three independent experiments were subjected to analysis by the automated image analysis program Motion Tracking (<http://motiontracking.mpi-cbg.de>). The cells were randomly selected for imaging. At least 15 images were acquired for each condition in a given experimental setup, and all the images were processed together for quantification. The objects were identified as vesicles in each channel based on their size, fluorescence intensity and other parameters by the automated Motion Tracking image analysis program. Objects detected in two different channels were considered to be colocalized if the relative overlap of respective areas was >35% (Rink et al., 2005; Collinet et al., 2010; Priya et al., 2015). The apparent colocalization value was calculated as the ratio of integral intensities of colocalized objects to the integral intensities of all objects carrying a given marker, and varied from 0.0 to 1.0. The colocalization-by-chance (random colocalization) was estimated by random permutation of objects localization in different channels. The apparent colocalization was corrected for random colocalization. Based on this method of calculating colocalization, we thereafter defined multicolor objects as those with a colocalization value greater than 0.35.

Live-cell imaging

Cells were co-transfected with GFP- and mCherry-fused proteins for 12 h, followed by trypsinization, and were seeded on glass-bottom dishes coated with gelatin. Cells in L-15 complete medium were incubated for 4 h at 37°C in an incubator and further imaged with an Olympus FV3000 confocal laser-scanning microscope with a 60 \times Plan Apo N objective (oil, 1.42 NA) on an inverted stage. Dual-color sequential imaging was performed using 488-nm and 561-nm lasers to excite GFP and mCherry fusion proteins, respectively. Images were acquired and processed using FV31S-SW software.

TIRF microscopy and analysis

Live-cell TIRF-M

To capture events specifically near the cell surface, images were captured with a Nikon Eclipse Ti2-E inverted microscope system equipped with H-TIRF setup and an on-stage incubation system with temperature and CO₂ controller (Okolab). Cells co-transfected with GFP and mCherry fusion proteins were plated on gelatin-coated, glass-bottom dishes filled with L-15 complete medium. Simultaneous dual-color imaging was performed using an Apo-TIRF 60 \times oil DIC N2 objective (oil, 1.49 NA), and a Nikon laser combiner LU-N4 (Nikon Corporation) with two Orca-Flash4.0 V3 sCMOS cameras (Hamamatsu Photonics). Image acquisition was performed with NIS-Elements AR 5.11.00. To excite GFP and mCherry, 488-nm and 561-nm lasers were used, respectively. Bandpass filters were selected to control fluorescence emission detection. Cells were transfected with siRNA or sgRNA, followed by pHluorin-fused MT1-MMP (Professor Philippe Chavrier) and images were acquired at an exposure time of 300–500 ms.

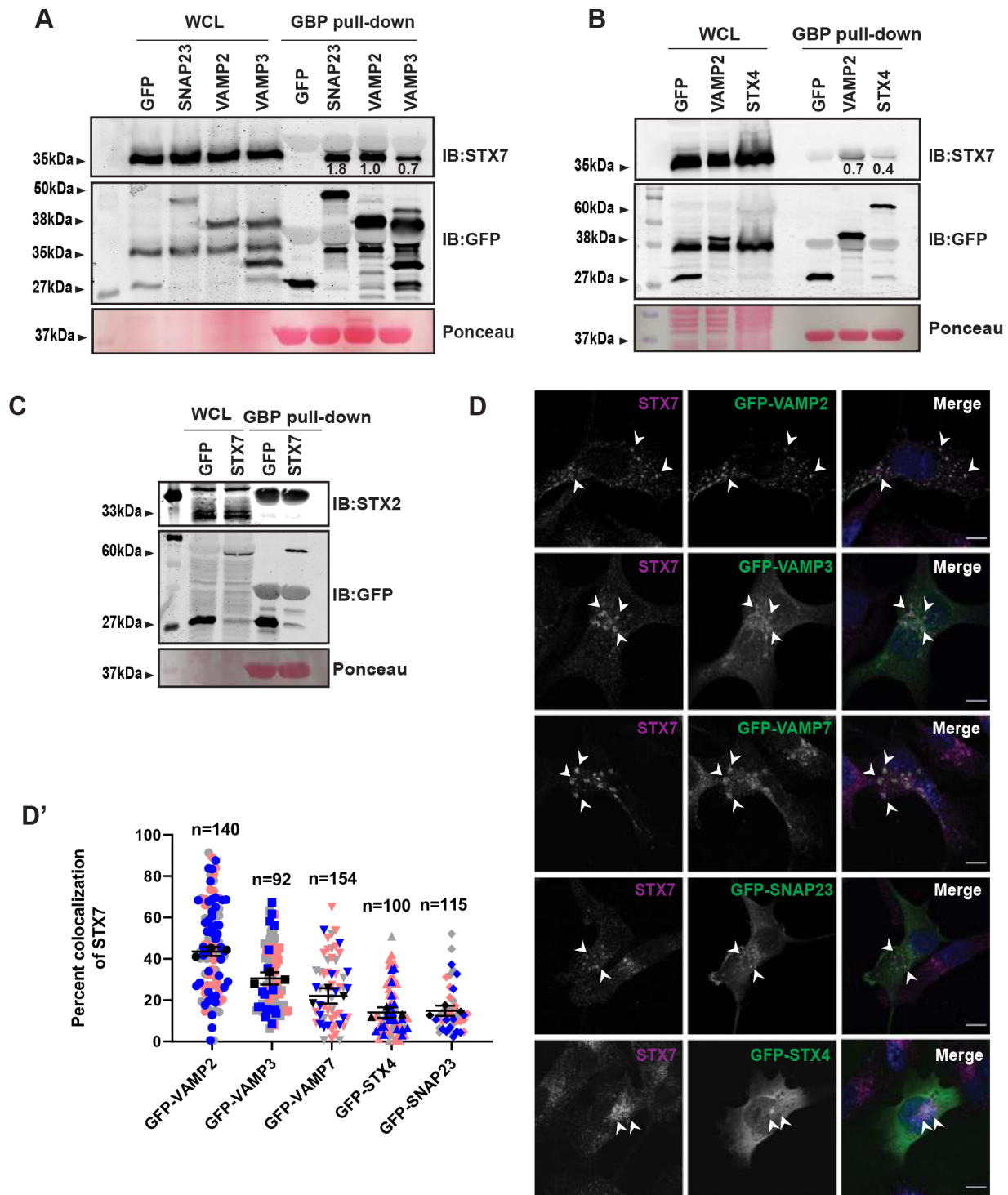


Fig. 5. STX7 interacts with multiple SNARE partners. (A) GBP pull-down was performed with lysates of HeLa cells expressing GFP-vector, and GFP-tagged SNAP23, VAMP2 and VAMP3, pre-treated with 1 mM NEM. Purified GST-GBP (25 μ g) was incubated with glutathione-Sepharose beads and allowed to bind with the respective lysates (300 μ g) for 5 h at 4°C. Beads were washed, boiled and advanced to immunoblotting using anti-STX7 and anti-GFP antibodies. The number represents the normalized value of prey protein (STX7) with respect to the precipitated protein (GFP-tagged protein) for the blot shown. WCL, whole-cell lysates. (B,C) GBP pull-down was performed with lysates from HEK-293 cells expressing GFP-vector, GFP-tagged VAMP2, STX4 and STX7, pre-treated with 1mM NEM. Purified GST-GBP (25 μ g) was incubated with glutathione-Sepharose beads and allowed to bind with the respective lysates from cells expressing GFP-vector (300 μ g), GFP-VAMP2 (300 μ g), GFP-STX4 (500 μ g) or GFP-STX7 (300 μ g) for 5 h at 4°C. Beads were washed, boiled and advanced to immunoblotting using anti-STX7, anti-STX2 and anti-GFP antibody. The number represents the normalized value of prey protein with respect to the precipitated protein (GFP-tagged protein) for the blot shown. Results in A–C are representative of three experimental repeats. (D) MDA-MB-231 cells with independent transfection of GFP-tagged VAMP2, VAMP3, VAMP7, SNAP23 or STX4 were immunostained for STX7. Arrowhead indicates colocalized puncta ($N=3$). Scale bars: 10 μ m. (D') Percentage colocalization was quantified and plotted. $N=3$, $n=140$ (GFP-VAMP2), $n=92$ (GFP-VAMP3), $n=154$ (GFP-VAMP7), $n=100$ (GFP-STX4), $n=115$ (GFP-SNAP23). The data are displayed using SuperPlots; each biological replicate is distinctly color-coded and each dot represents identified percentage colocalization in a field of view (frame), as described in the Materials and Methods, with mean \pm s.d. N , number of experimental repeats; n , number of cells analyzed.

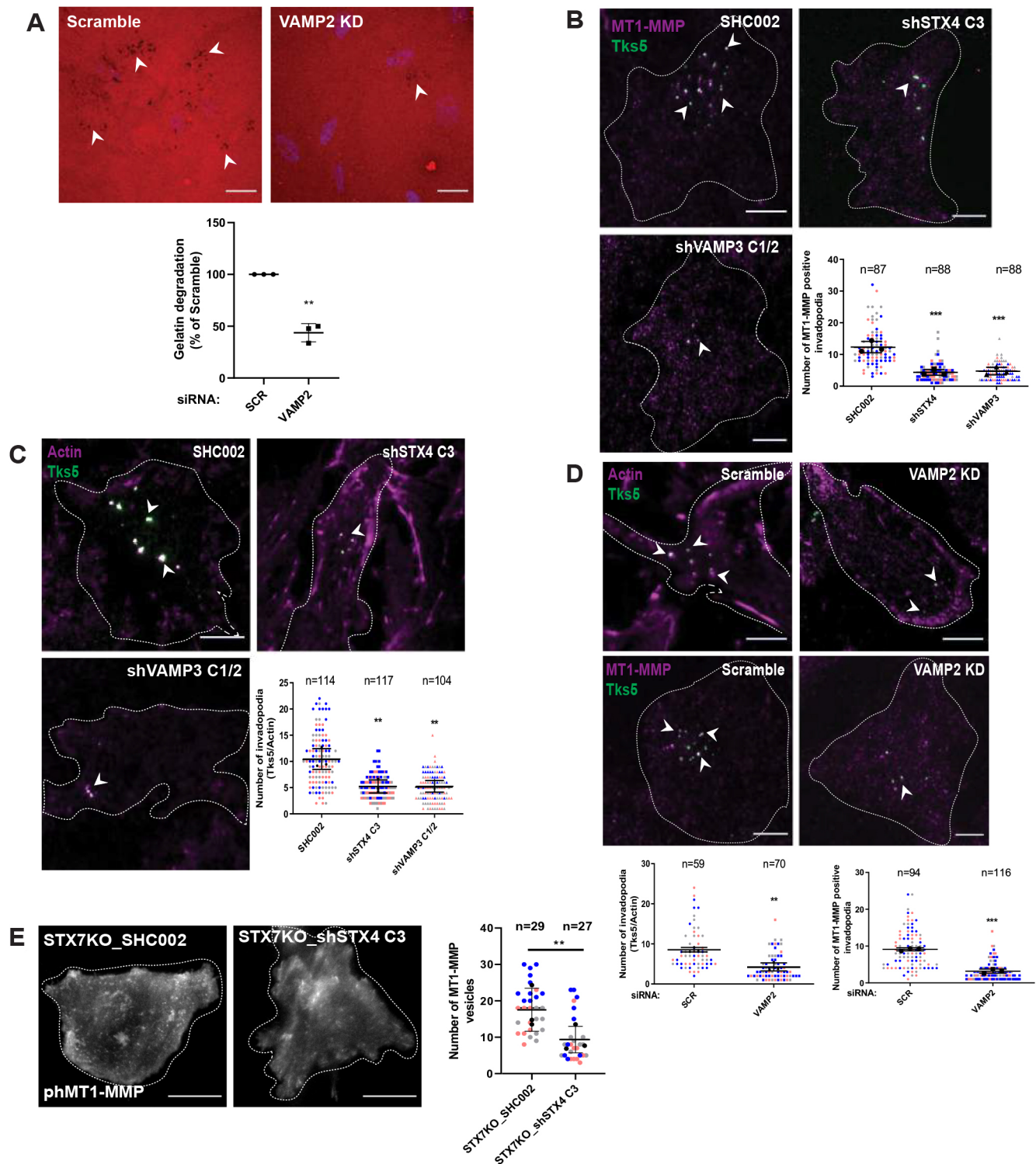


Fig. 6. See next page for legend.

The number of MT1-MMP vesicles that are available in the TIRF plane and could form a track spanning a minimum of four consecutive frames in live-cell TIRF video captured over 1 min duration was quantified.

Detailed steps involved in quantification are as follows:

(1) Object identification. Object-based analysis was performed by the automated image analysis program Motion Tracking (<http://motiontracking.mpi-cbg.de>; Rink et al., 2005; Collinet et al., 2010). The core of Motion Tracking is finding the position of objects in the acquired frames of the movie, such as a fluorescent molecule. Once found, the software assigns an

x-y position and quantifies the intensity profiles of the objects. Each object is basically a group of pixels. The number of pixels combined with the scale will lead to 'object size' and 'area' determination. Each pixel has its own brightness called 'intensity'. The vesicles are identified as objects by setting parameters.

(2) Identifying the tracks. Once Motion Tracking has successfully localized every object in the movie, the objects in consecutive frames can be linked into trajectories, or tracks. A track is the location of an object over time. Tracks have properties such as speed, direction, maximum

Fig. 6. Interacting partners could phenocopy the STX7. (A) MDA-MB-231 cells were transfected with the indicated siRNA (SHC002 is a control shRNA). At 60 h post transfection, cells were seeded on Alexa Fluor 568-labeled gelatin-coated coverslips for 12 h. Arrowheads indicate the degradation spot. Images were acquired randomly, and degradation activity was quantified and plotted ($N=3$, $n\geq 300$). $**P<0.01$ (unpaired two-tailed Student's *t*-test). (B) MDA-MB-231 cells treated with control, STX4 and VAMP3 shRNA were seeded on an unlabeled gelatin-coated coverslip, and immunostained for Tks5 and MT1-MMP. Images were acquired using fixed-cell TIRF-M. Arrowhead indicates colocalized puncta at the surface. The number of MT1-MMP-positive Tks5 structures were counted and plotted. $N=3$, $n=87$ (SHC002), $n=88$ (shSTX4), $n=88$ (shVAMP3). $***P<0.001$ (one-way ANOVA with Dunnett's multiple comparisons test). (C) MDA-MB-231 cells treated with control, STX4 and VAMP3 shRNA were seeded on an unlabeled gelatin-coated coverslip, immunostained for Tks5 and labelled with Phalloidin-568. Images were acquired using a fixed cell TIRF-M. Arrowhead indicates colocalized puncta at the surface. The number of invadopodia was quantified and plotted. $N=3$, $n=114$ (SHC002), $n=117$ (shSTX4), $n=104$ (shVAMP3). $**P<0.01$ (one-way ANOVA with Dunnett's multiple comparisons test). (D) MDA-MB-231 cells were transfected with control siRNA and siRNA targeting VAMP2. After 72 h of transfection, cells were immunostained with Tks5-phalloidin-568 or for Tks5 and MT1-MMP, then subjected to TIRF imaging. Arrowheads indicate colocalized puncta at the surface. The number of invadopodia and the number of MT1-MMP-positive Tks5 structures were counted and plotted. $N=3$; for Tks5 and actin staining, $n=59$ (Scr), $n=70$ (VAMP2); for Tks5 and MT1-MMP staining, $n=94$ (Scr), $n=116$ (VAMP2). $**P<0.01$, $***P<0.001$ (unpaired two-tailed Student's *t*-test). (E) MDA-MB-231 STX7KO cells were transfected with SHC002 (control) and shSTX4, and post depletion cells were transfected with pHMT1-MMP. Transfected cells were seeded on a gelatin-coated surface and subjected to TIRF imaging ($N=3$). $**P<0.01$ (unpaired two-tailed Student's *t*-test). For data that are displayed using SuperPlots, each biological replicate is distinctly color-coded and each dot represents an identified multicolor object in a field of view (frame) or track formed in a movie, as described in the Materials and Methods. All the graphs represent means \pm s.d. *N*, number of experimental repeats; *n*, number of cells analyzed. Dotted line highlights cell edge. All scale bars: 10 μ m.

displacement, intensity and area that are adjusted to identify tracks. The relative weights can take any positive values from 0 to 1.

(3) Setting track break thresholds. To adjust the track break thresholds, the same dialogue box is used. Parameters are: total score threshold, area score threshold, intensity score threshold, and integral score threshold. These thresholds are critical as they will command the program to select a range of the variation in properties of the object that it can tolerate while building a track.

(4) Searching of tracks in the entire movie.

(5) Quantifying the number of vesicles near the cell surface. This is the number of tracks detected in a 1 min movie. Each of the tracks identified using above method are considered as an MT1-MMP vesicle near the TIRF surface.

Fixed-cell TIRF-M

Fixed-cell TIRF-M was performed by plating the siRNA- or shRNA-treated cells over a gelatin-coated glass-bottom dish for 8 h or 4 h, respectively, followed by fixation using 4% PFA, permeabilization with 0.1% Triton X-100 for 10 min at room temperature, and blocking with 5% FBS in 1 \times PBS before staining with respective antibodies. Finally, after staining, the cells were kept in 1 \times PBS for performing TIRF imaging. Z-stack images of the fixed samples were acquired with z-step of 0.02 μ m, with total step count of 51. Deconvolution was performed using the Richardson–Lucy method with 20 iterations with NIS-Element AR 5.11.00 software. Acquired images were searched for multicolor objects (as described above) using the automated image analysis program Motion Tracking.

MT1-MMP antibody uptake assay

MDA-MB-231 cells were trypsinized and counted, and 30,000 cells per well were seeded on the gelatin-coated coverslips for 24 h and transfected with siRNA. After 72 h of transfection, antibody uptake was performed using anti-MT1-MMP antibody (R&D Systems, MAB9181-SP). Cells were incubated at 4°C with 10 μ g ml⁻¹ anti-MT1-MMP antibody diluted in serum-free L-15 medium for 1 h. The unbound antibody was removed by

washing with 1 \times PBS. L-15 complete medium was added, and cells were shifted to 37°C to allow internalization of the surface-bound antibody. At the 15-min time point, cells were fixed by adding 4% PFA, followed by staining with DAPI.

Transferrin pulse-chase

MDA-MB-231 cells were trypsinized and counted, and 30,000 cells per well were seeded for 24 h and transfected with siRNA. Cells were incubated at 4°C with 10 μ g ml⁻¹ Alexa Fluor 568-labeled transferrin diluted in L-15 serum-free medium for 1 h. The unbound antibody was removed after washing with 1 \times PBS. L-15 complete medium was added, and cells were shifted to 37°C to allow internalization for 5 and 10 min. Cells were fixed by adding 4% PFA, followed by staining with DAPI.

Similarly, HeLa cells were transfected with siRNA. After 70 h of knockdown, cells were serum starved for 2 h and pulse labeled with Alexa Fluor-568-conjugated transferrin (20 μ g/ml) diluted in serum-free DMEM (SFM) for 1 h at 4°C. Cells were washed with 1 \times PBS to remove unbound transferrin. Alexa Fluor 568–transferrin-labeled surface receptors were chased in the presence of holotransferrin (100 μ g/ml) diluted in L-15 SFM for different time points. At each time point, cells were quickly washed and fixed using 4% PFA and further proceeded for immunofluorescence.

Gelatin degradation assay

MDA-MB-231, MDA-MB-468 and MCF10DCIS.com cells after 60 h of transfection were trypsinized and 50,000 cells were plated on Alexa Fluor 568-labeled fluorescent gelatin for 12 h. Cells were then fixed and stained with DAPI. Images were captured using a Zeiss LSM780 confocal laser scanning microscope with a 40 \times 1.4 NA oil immersion objective. Images were processed in the Motion Tracking software, where degradation area was identified as an object and the degradation index was calculated as described in Sharma et al. (2020).

Matrigel invasion assay

The Matrigel invasion assay was performed by transfecting MDAMB-231 cells with 20 nM siRNA targeting the gene of interest. After 60 h of transfection, cells were trypsinized and counted, and 50,000 cells were resuspended in serum-free medium and seeded on BD Transwell cell inserts (8- μ m pore size) coated with 0.5 mg ml⁻¹ of Matrigel (BD Biosciences, Cat. 354277). Complete medium with 10% FBS was added to the lower chamber. Transwell plates were kept at 37°C for 16–18 h. Cells on the inserts were fixed with 4% PFA for 20 min, and washed three times with 1 \times PBS. Non-invaded cells were removed using a cotton swab. Inserts were dried for 6 h at room temperature and imaged using an inverted epifluorescence microscope using a 10 \times objective in bright field mode. Cells were counted using ImageJ software.

Pervanadate treatment

Cells were treated with a pervanadate/H₂O₂ mixture; for this, 1 ml of a 20 mM sodium orthovanadate stock solution was mixed with 330 μ l of 30% H₂O₂ and incubated for 5 min at room temperature, yielding a solution of 6 mM pervanadate plus remaining H₂O₂. To stimulate cells with 40 μ M pervanadate/H₂O₂, the prepared solution was diluted 1:5 with H₂O, and 16 μ l of this solution was diluted in 2 ml of serum-free L-15 medium, and 500 μ l was added to each well containing 3 \times 10⁵ cells. As pervanadate/H₂O₂ is unstable, a fresh solution was prepared each time. Cells were treated with pervanadate for 30 min at 37°C. Approximately 20 s before the end of the desired time, cells were pelleted (12,000 *g* for 4 min) and lysed using lysis buffer consisting of 137 mM NaCl, 50 mM Tris-HCl (pH 7.8), 10% (v/v) glycerol, 1 mM sodium orthovanadate, 2 mM EDTA (pH 8.0), 1% vol/vol Nonidet P-40, plus protease inhibitors leupeptin and aprotinin (10 μ g/ml each; Sigma), and 1 mM PMSF. Cell debris was spun down for 15 min at 19,000 *g* at 4°C and cleared cellular lysates were analyzed by anti-phosphotyrosine immunoblotting (Wienands et al., 1996; Cory et al., 2002).

MT1-MMP surface biotinylation

To measure the surface population, MDA-MB-231 cells (9 \times 10⁴ cells per ml) were grown in a 35-mm plate for 24 h. Cells were then transfected with

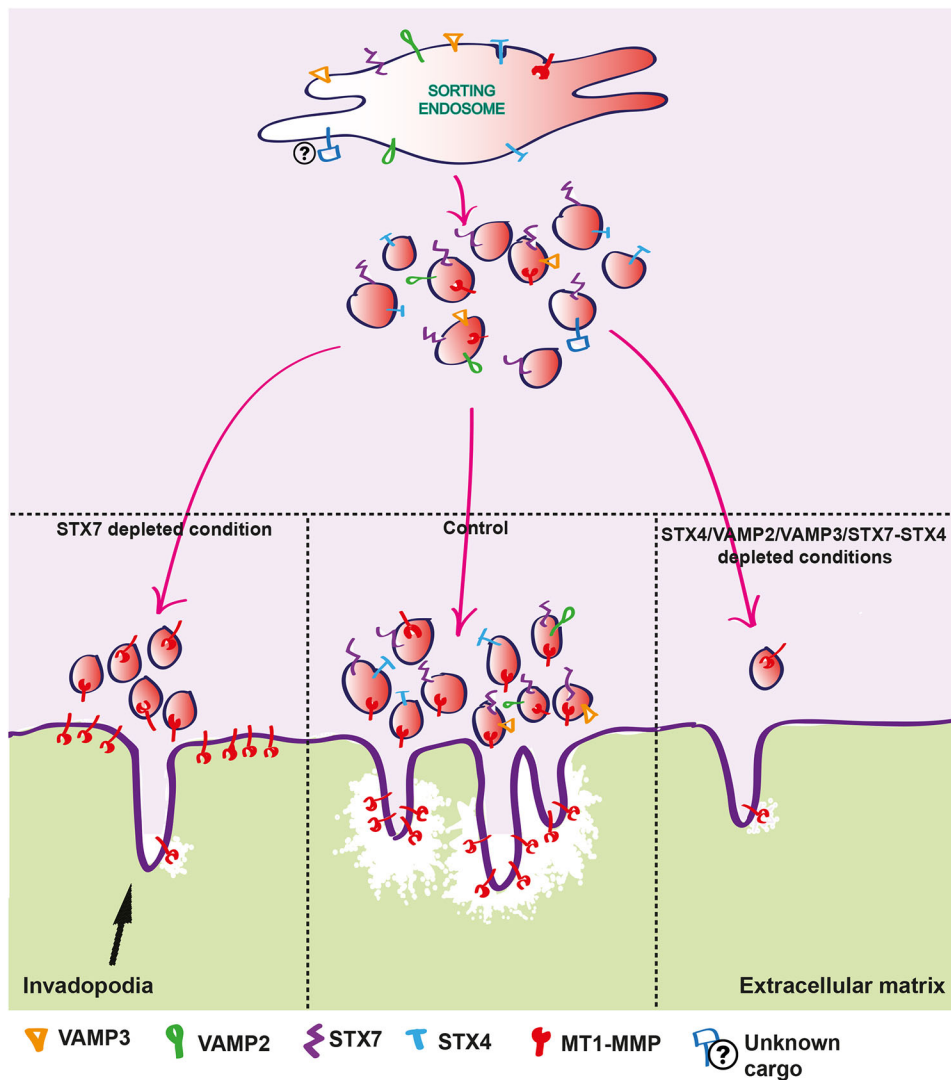


Fig. 7. The proposed model showing that STX7 interacts with multiple SNAREs and forms multiple distinct SNARE complexes. These complexes assist in the fusion of vesicles carrying MT1-MMP to invadopodia, thus, facilitating ECM degradation. However, upon depletion of STX7, trafficking of MT1-MMP is diverted towards the PM rather than invadopodia. Also, silencing of STX7 abrogates the formation of invadopodia, possibly due to hampered trafficking of signaling molecules or growth factors or an unknown cargo carried by STX7 to promote invadopodia formation. Alternatively, when STX4, VAMP2, VAMP3 or STX7-STX4 is depleted, there is reduced MT1-MMP trafficking to cell surface as well as reduced invadopodia formation.

siRNA. At the 72-h post-transfection time point, biotinylation was performed. The culture medium was removed and the cells were washed carefully with 2 ml PBS (6.7 mM NaHPO₄, 3.3 mM NaH₂PO₄, and 140 mM NaCl, pH 7.2) and incubated with EZ-link Sulfo-NHS-Biotin (Invitrogen, Cat. 21217) at 4°C for 45 min. Further, to quench unreacted biotin, cells were treated with a quenching solution (50 mM Tris-HCl, pH 8.0). After quenching, cells were washed with 1× PBS and solubilized in lysis buffer. The lysate was incubated with Neutravidin beads (Pierce, Cat. 29200) for 30 min at room temperature. Biotin-labeled proteins were eluted from the beads and subjected to immunoblotting. The intensity of the biotinylated MT1-MMP was quantified for Scrambled (Scr) and siRNA-treated samples for STX7 using ImageJ software. The scanned western blot image was converted into a grayscale image for densitometric analysis (Sharma et al., 2020).

To measure endocytosis, cells were transfected with siRNA as mentioned above, and surface proteins were labelled with cleavable biotin and EZ-Link Sulfo-NHS-SS-Biotin (0.2 mgml⁻¹; Invitrogen, 21331) for 45 min at 4°C. Unreacted biotin was quenched with the quenching solution. After quenching, cells were washed with 1× PBS and solubilized in lysis buffer (0 min MeSNa⁻). In parallel, one set was proceed for MeSNa treatment i.e. 50 mM MeSNa in MeSNa buffer [50 mM Tris-HCl, pH 8.0, 100 mM NaCl, 1 mM EDTA and 0.2 (w/v) BSA, pH 8.6] to remove biotin-labeled proteins, followed by quenching (0 min MeSNa⁺) after which cells were solubilized. To measure internalization, cells were allowed to endocytose biotinylated proteins at 37°C for 15 min and then shifted to 4°C. After 15 min of endocytosis (15 min, MeSNa⁻), cells were immediately lysed to measure

the total biotinylated population. However, other cells were washed and given MeSNa treatment followed by quenching to remove non-internalized population (15 min, MeSNa⁺). Cells were solubilized in the lysis buffer to measure the endocytosed population. The biotin-labeled proteins (lysate) were incubated with Neutravidin beads (Pierce, Cat. 29200) for 30 min at room temperature and eluted by boiling the beads in 2× SDS loading dye. Immunoblotting was performed to detect protein levels. The percentage of endocytosis was calculated as: amount endocytosed at time 15 min (t_{15}) = B/A , where A = intensity at t_{15} (MeSNa⁻) after background subtraction, and B = intensity at t_{15} (MeSNa⁺) after background subtraction.

NEM treatment and GFP-trap pull down

pGEX6P1-GFPNanobody was purchased from Addgene (Addgene #61838). The GFP-binding protein (GBP) clone was further subcloned into a pGEX-6P1 vector for improved expression of GST-tagged GBP. GFP-Vector or GFP fusion proteins were overexpressed in a six-well format in the cell line. 16 h after transfection, cells were treated with *N*-ethylmaleimide (NEM; 1 mM) diluted in 1× PBS for 15 min at 4°C, followed by 1 mM NEM diluted in complete medium at 37°C for 30 min. Cells were lysed in 20 mM Tris-HCl, pH 8.0, 137 mM NaCl, 10% glycerol, 2 mM EDTA, and 1% NP-40, and cleared by centrifuging at 19,000 *g* at 4°C for 15 min. Cleared lysates were mixed with 25 µg of GST-GBP and bound to the glutathione sepharose beads. The beads bound with GBP-GFP protein complexes were then washed three times with PBS, followed by elution using 2× SDS sample loading buffer. Samples were then separated over 12% SDS-PAGE followed by western blotting. Protein transferred over

nitrocellulose membrane was sequentially probed with anti-STX7 or anti-STX2, and anti-GFP antibodies.

Western blotting

Cells were harvested and lysed in lysis buffer (50 mM Tris-HCl pH 7.4, 150 mM NaCl, 2 mM DTT, 1% Triton X-100, and 1 mM EDTA) supplemented with 10 µg ml⁻¹ protease inhibitor cocktail (PIC, Sigma). Cell debris was removed by centrifuging at 19,000 *g* for 15 min at 4°C. Protein concentration was estimated using the Bradford assay. Samples were prepared by adding 1× SDS loading dye and separated by running on SDS-PAGE, then transfer to a nitrocellulose membrane (0.45 µm; GE Healthcare, Cat. 10600002). The membrane was blocked with 5% BSA, then incubated for 1 h at room temperature with the respective primary antibody. To detect the bound antibody signal, the membrane was incubated with fluorescently labelled secondary antibody, and protein bands were detected using the Li-Cor Odyssey Infrared Scanning System. The uncropped blots of main western blots are provided in Fig. S5.

Generation of STX7KO and STX7KO-NC cell lines using CRISPR/Cas9

Using an online CRISPR design tool (<https://www.thermofisher.com/in/en/home/life-science/genome-editing/geneart-crispr/crispr-libraries/trueguide-grnas.html>) from Thermo Fisher Scientific, a 20-nucleotide guide sequence was designed against human STX7. The targeted DNA sequence was the G*G*A*UGUUAGAAGAGAUCCUC+ modified scaffold. A negative control non-targeting single gRNA (sgRNA) 5'-AAAUGUGAGAUCA-GAGUAAU-3' that does not recognize any specific sequence was also used. To generate the clonal cell line, 1000 cells per well were seeded for 24 h before transfection in a 96-well plate. Cells were transfected with Cas9-sgRNA complex at a ratio of 250 ng per 1.5 pmol per protein using Lipofectamine Cas9 plus (Invitrogen, Cat. A36496) and Lipofectamine CRISPRMAX (Invitrogen, Cat. CMAX00003) reagents. At 48 h after transfection, cells were serially diluted to single cells and grown until they reached 80% confluency. CRISPR knockout was confirmed by western blotting. To generate the non-clonal cell line, 1000 cells per well were seeded for 24 h before transfection in a 96-well plate. Cells were transfected as described above, and at 48 h after transfection, transfection reagent was removed and cells were grown until they reached 80% confluency. CRISPR knockout was confirmed by western blotting.

Statistical analysis

For the statistical evaluation of the datasets from quantitative image analysis, paired or unpaired two-tailed Student's *t*-test or one-way ANOVA with a Dunnett's multiple comparisons test was performed using GraphPad Prism 6 and 8 software version 6.01 and 8.0.2, respectively. Datasets are presented as mean±s.d. For the data that are displayed using SuperPlots, each biological replicate is distinctly color-coded and each dot represents percentage colocalization for identified multicolor objects or number of identified multicolor objects in a field of view (frame). One frame comprises 1–3 cells, contributing to a total number of cells (*n*) across the total number of frames acquired. The frame-wise values were separately pooled for each biological replicate to calculate the mean in the SuperPlots and the s.d. represents the deviation of the data from these three means (Lord et al., 2020). The significance is as follows: *P*>0.05, ns (non-significant), **P*≤0.05, ***P*≤0.01, ****P*≤0.001 and *****P*≤0.0001. The number of samples, images and experiments used for quantification are mentioned in the respective figure legends or in figures. In all figures, *n*=number of cells and *N*=number of experiments.

Acknowledgements

We thank Professor Philippe Chavrier [Centre National de la Recherche Scientifique (CNRS), Paris, France] for sharing pCDNA3.1 MT1-MMP pHuorin construct and the MCF10DCIS.com line; Professor Marino Zerial (Max Planck Institute, Dresden, Germany) for sharing EEA1 antibody, the pEGFP-C1 Rab4 construct, the pEGFP-C3 Rab11 construct; Professor Reinhard Jahn (Max Planck Institute for Biophysical Chemistry, Göttingen, Germany) for sharing the rat STX7Cyt construct; Professor Andrew Peden (University of Sheffield, South Yorkshire, England) for sharing the protocol for SNAREs interaction and the HA-VAMP3 construct; and Professor Ludger Johannes (Institut Curie, Paris, France) for sharing the pEGFP-C2-VAMP2-

myc construct. We thank Professor Sanjeev Shukla (IISERB) for providing us the MDA-MB-468 cell line. We are thankful to the Central Instrumentation Facility at IISER Bhopal that was used to perform confocal and TIRF microscopy-based experiments. We also acknowledge the FIST facility at IISER Bhopal by DST for providing facility to conduct live-cell imaging-based experiments. We sincerely thank Dr Dipanjan Ghosh (IISERB) Dr Amulya Priya (France), Dr Priyanka Sharma (IISERB) for critically analyzing the manuscript and insightful suggestions. We also thank Dr Ebsy Jaimon (IISERB), Ms Achala Apte (IISERB) for suggestions in the manuscript and Rabiya Naaz for lab management.

Competing interests

The authors declare no competing or financial interests.

Author contributions

Conceptualization: S.P., S.D.; Methodology: S.P.; Validation: S.P., S.D.; Formal analysis: S.P., A.K., S.D.; Investigation: S.P., A.K.; Resources: S.P., J.R., M.G.C., S.D.; Data curation: S.D.; Writing - original draft: S.P.; Writing - review & editing: M.G.C., S.D.; Visualization: S.P., S.D.; Supervision: S.D.; Project administration: S.P.; Funding acquisition: S.D.

Funding

This work was funded by the Ministry of Human Resources and Development, India (MHRD; MHRD/BIO/2019047). The project was also funded by Science and Engineering Research Board (CRG/2019/004580). S.P. was supported by a MHRD fellowship.

Peer review history

The peer review history is available online at <https://journals.biologists.com/jcs/article-lookup/doi/10.1242/jcs.259576>.

References

- Achuthan, A., Masendycz, P., Lopez, J. A., Nguyen, T., James, D. E., Sweet, M. J., Hamilton, J. A. and Scholz, G. M. (2008). Regulation of the endosomal SNARE protein syntaxin 7 by colony-stimulating factor 1 in macrophages. *Mol. Cell. Biol.* **28**, 6149–6159. doi:10.1128/MCB.00220-08
- Alexander, N. R., Branch, K. M., Parekh, A., Clark, E. S., Iwueke, I. C., Guelcher, S. A. and Weaver, A. M. (2008). Extracellular matrix rigidity promotes invadopodia activity. *Curr. Biol.* **18**, 1295–1299. doi:10.1016/j.cub.2008.07.090
- Artym, V. V., Zhang, Y., Seillier-Moisewitsch, F., Yamada, K. M. and Mueller, S. C. (2006). Dynamic interactions of cortactin and membrane type 1 matrix metalloproteinase at invadopodia: Defining the stages of invadopodia formation and function. *Cancer Res.* **66**, 3034–3043. doi:10.1158/0008-5472.CAN-05-2177
- Ayala, I., Baldassarre, M., Giacchetti, G., Caldieri, G., Tete, S., Luini, A. and Buccione, R. (2008). Multiple regulatory inputs converge on cortactin to control invadopodia biogenesis and extracellular matrix degradation. *J. Cell Sci.* **121**, 369–378. doi:10.1242/jcs.008037
- Beatty, B. T., Sharma, V. P., Bravo-Cordero, J. J., Simpson, M. A., Eddy, R. J., Koleske, A. J. and Parent, C. (2013). β1 integrin regulates Arg to promote invadopodial maturation and matrix degradation. *Mol. Biol. Cell* **24**, 1661–1675. doi:10.1091/mbc.e12-12-0908
- Bilan, F., Nacfer, M., Fresquet, F., Norez, C., Melin, P., Martin-Berge, A., Costa De Beauregard, M.-A., Becq, F., Kitzis, A. and Thoreau, V. (2008). Endosomal SNARE proteins regulate CFTR activity and trafficking in epithelial cells. *Exp. Cell Res.* **314**, 2199–2211. doi:10.1016/j.yexcr.2008.04.012
- Bonifacio, J. S. and Glick, B. S. (2004). Review the mechanisms of vesicle budding and fusion of the pathway. Such observations inspired the vesicular transport hypothesis, which states that the transfer of cargo molecules between organelles of the. *Cell* **116**, 153–166. doi:10.1016/S0092-8674(03)01079-1
- Brasher, M. I., Martynowicz, D. M., Grafinger, O. R., Hucik, A., Shanks-Skinner, E., Uniacke, J. and Coppolino, M. G. (2017). Interaction of Munc18c and syntaxin4 facilitates invadopodium formation and extracellular matrix invasion of tumor cells. *J. Biol. Chem.* **292**, 16199–16210. doi:10.1074/jbc.M117.807438
- Cai, H., Reinisch, K. and Ferro-Novick, S. (2007). Coats, tethers, Rabs, and SNAREs work together to mediate the intracellular destination of a transport vesicle. *Dev. Cell* **12**, 671–682. doi: 10.1016/j.devcel.2007.04.005
- Castro-Castro, A., Marchesin, V., Monteiro, P., Lodillinsky, C., Rossé, C. and Chavrier, P. (2016). Cellular and molecular mechanisms of MT1-MMP-dependent cancer cell invasion. *Annu. Rev. Cell Dev. Biol.* **32**, 555–576. doi: 10.1146/annurev-cellbio-111315-125227
- Cepeda, M. A., Pelling, J. J. H., Evered, C. L., Williams, K. C., Freedman, Z., Stan, I., Willson, J. A., Leong, H. S. and Damjanovski, S. (2016). Less is more: Low expression of MT1-MMP is optimal to promote migration and tumourigenesis of breast cancer cells. *Mol. Cancer* **15**, 65. doi: 10.1186/s12943-016-0547-x
- Chun, T.-H., Sabeh, F., Ota, I., Murphy, H., McDonagh, K. T., Holmbeck, K., Birkedal-Hansen, H., Allen, E. D. and Weiss, S. J. (2004). MT1-MMP-

- dependent neovessel formation within the confines of the three-dimensional extracellular matrix. *J. Cell Biol.* **167**, 757–767. doi:10.1083/jcb.200405001
- Clancy, J. W., Sedgwick, A., Rosse, C., Muralidharan-Chari, V., Raposo, G., Method, M., Chavrier, P. and D'Souza-Schorey, C. (2015). Regulated delivery of molecular cargo to invasive tumour-derived microvesicles. *Nat. Commun.* **6**, 6919. doi:10.1038/ncomms7919
- Clark, E. S., Whigham, A. S., Yarbrough, W. G. and Weaver, A. M. (2007). Cortactin is an essential regulator of matrix metalloproteinase secretion and extracellular matrix degradation in invadopodia. *Cancer Res.* **67**, 4227–4235. doi:10.1158/0008-5472.CAN-06-3928
- Clark, E. S. and Weaver, A. M. (2008). A new role for cortactin in invadopodia: regulation of protease secretion. *Eur. J. Cell Biol.* **87**, 581–590. doi:10.1016/j.ejcb.2008.01.008
- Collinet, C., Stöter, M., Bradshaw, C. R., Samusik, N., Rink, J. C., Kenski, D., Habermann, B., Buchholz, F., Henschel, R., Mueller, M. S. et al. (2010). Systems survey of endocytosis by multiparametric image analysis. *Nature* **464**, 243–249. doi:10.1038/nature08779
- Cory, G. O. C., Garg, R., Cramer, R. and Ridley, A. J. (2002). Phosphorylation of tyrosine 291 enhances the ability of WASp to stimulate actin polymerization and filopodium formation. Wiskott-Aldrich Syndrome protein. *J. Biol. Chem.* **277**, 45115–45121. doi:10.1074/jbc.M203346200
- Destaing, O., Planus, E., Bouvard, D., Oddou, C., Badowski, C., Bossy, V., Raducanu, A., Fourcade, B., Albiges-Rizo, C. and Parent, C. (2010). A integrin is a master regulator of invadosome organization and function. *Mol. Biol. Cell* **21**, 4108–4119. doi:10.1091/mbc.e10-07-0580
- Even-Ram, S. and Yamada, K. M. (2005). Cell migration in 3D matrix. *Curr. Opin. Cell Biol.* **17**, 524–532. doi:10.1016/j.ccb.2005.08.015
- Feldmann, A., Winterstein, C., White, R., Trotter, J. and Krämer-Albers, E.-M. (2009). Comprehensive analysis of expression, subcellular localization, and cognate pairing of SNARE proteins in oligodendrocytes. *J. Neurosci. Res.* **87**, 1760–1772. doi:10.1002/jnr.22020
- Ferrari, R., Martin, G., Tagit, O., Guichard, A., Cambi, A., Voituriez, R., Vassilopoulos, S. and Chavrier, P. (2019). MT1-MMP directs force-producing proteolytic contacts that drive tumor cell invasion. *Nat. Commun.* **10**, 4886. doi:10.1038/s41467-019-12930-y
- Friedl, P., Maaser, K., Klein, C. E., Niggemann, B., Krohne, G. and Zänker, K. S. (1997). Migration of highly aggressive MV3 melanoma cells in 3-dimensional collagen lattices results in local matrix reorganization and shedding of alpha2 and beta1 integrins and CD44. *Cancer Res.* **57**, 2061–2070.
- Frittoli, E., Palamidessi, A., Disanza, A. and Scita, G. (2011). Secretory and endo/exocytic trafficking in invadopodia formation: the MT1-MMP paradigm. *Eur. J. Cell Biol.* **90**, 108–114. doi:10.1016/j.ejcb.2010.04.007
- Frittoli, E., Palamidessi, A., Marighetti, P., Confalonieri, S., Bianchi, F., Malinverno, C., Mazzarol, G., Viale, G., Martin-Padura, I., Garré, M. et al. (2014). A RAB5/RAB4 recycling circuitry induces a proteolytic invasive program and promotes tumor dissemination. *J. Cell Biol.* **206**, 307–328. doi:10.1083/jcb.201403127
- Gordon, D. E., Mirza, M., Sahlender, D. A., Jakovleska, J. and Peden, A. A. (2009). Coiled-coil interactions are required for post-Golgi R-SNARE trafficking. *EMBO Rep.* **10**, 851–856. doi:10.1038/embo.2009.96
- Hasan, N. and Hu, C. (2010). Vesicle-associated membrane protein 2 mediates trafficking of $\alpha 5 \beta 1$ integrin to the plasma membrane. *Exp. Cell Res.* **316**, 12–23. doi:10.1016/j.yexcr.2009.10.007
- Hayes, K. E., Walk, E. L., Ammer, A. G., Kelley, L. C., Martin, K. H. and Weed, S. A. (2013). Ablation of kinases negatively regulate invadopodia function and invasion in head and neck squamous cell carcinoma by inhibiting an HB-EGF autocrine loop. *Oncogene* **32**, 4766–4777. doi:10.1038/onc.2012.513
- Heng Wong, S., Xu, Y., Zhang, T. and Hong, W. (1998). Syntaxin 7, a novel syntaxin member associated with the early endosomal compartment. *J. Biol. Chem.* **273**, 375–380. doi:10.1074/jbc.273.1.375
- Hong, W. (2005). SNAREs and traffic. *Biochim. Biophys. Acta* **1744**, 493–517. doi:10.1016/j.bbamcr.2005.03.014
- Itoh, Y. (2015). Membrane-type matrix metalloproteinases: Their functions and regulations. *Matrix Biol.* **44–46**, 207–223. doi:10.1016/j.matbio.2015.03.004
- Jabłońska-Trypuć, A., Matejczyk, M. and Rosochacki, S. (2016). Matrix metalloproteinases (MMPs), the main extracellular matrix (ECM) enzymes in collagen degradation, as a target for anticancer drugs. *J. Enzyme Inhib. Med. Chem.* **31**, 177–183. doi:10.3109/14756366.2016.1161620
- Jacob, A. and Prekeris, R. (2015). The regulation of MMP targeting to invadopodia during cancer metastasis. *Front. Cell Dev. Biol.* **3**, 4. doi:10.3389/fcell.2015.00004
- Jahn, R. and Scheller, R. H. (2006). SNAREs – Engines for membrane fusion. *Nat. Rev. Mol. Cell Biol.* **7**, 631–643. doi:10.1038/nrm2002
- Jeannot, P. and Besson, A. (2020). Cortactin function in invadopodia. *Small GTPases* **11**, 256–270. doi:10.1080/21541248.2017.1405773
- Jia, Y. L., Shi, L., Zhou, J.-N., Fu, C.-J., Chen, L., Yuan, H.-F., Wang, Y.-F., Yan, X.-L., Xu, Y.-C., Zeng, Q. et al. (2011). Epimorphin promotes human hepatocellular carcinoma invasion and metastasis through activation of focal adhesion kinase/extracellular signal-regulated kinase/matrix metalloproteinase-9 axis. *Hepatology* **54**, 1808–1818. doi:10.1002/hep.24562
- Kajiho, H., Kajiho, Y., Frittoli, E., Confalonieri, S., Bertalot, G., Viale, G., Di Fiore, P. P., Oldani, A., Garre, M., Beznoussenko, G. V. et al. (2016). RAB2A controls MT1-MMP endocytic and E-cadherin polarized Golgi trafficking to promote invasive breast cancer programs. *EMBO Rep.* **17**, 1061–1080. doi:10.15252/embr.201642032
- Kasai, K. and Akagawa, K. (2001). Roles of the cytoplasmic and transmembrane domains of syntaxins in intracellular localization and trafficking. *J. Cell Sci.* **114**, 3115–3124. doi:10.1242/jcs.114.17.3115
- Kawauchi, T. (2012). Cell adhesion and its endocytic regulation in cell migration during neural development and cancer metastasis. *Int. J. Mol. Sci.* **13**, 4564–4590. doi:10.3390/ijms13044564
- Kean, M. J., Williams, K. C., Skalski, M., Myers, D., Burtinik, A., Foster, D. and Coppolino, M. G. (2009). VAMP3, syntaxin-13 and SNAP23 are involved in secretion of matrix metalloproteinases, degradation of the extracellular matrix and cell invasion. *J. Cell Sci.* **122**, 4089–4098. doi:10.1242/jcs.052761
- Kessenbrock, K., Plaks, V. and Werb, Z. (2010). Matrix metalloproteinases: regulators of the tumor microenvironment. *Cell* **141**, 52–67. doi:10.1016/j.cell.2010.03.015
- Kim, M.-C., Li, R., Abeyaratne, R., Kamm, R. D. and Asada, H. H. (2022). A computational modeling of invadopodia protrusion into an extracellular matrix fiber network. *Sci. Rep.* **12**, 1231. doi:10.1038/s41598-022-05224-9
- Kubo, K., Kobayashi, M., Nozaki, S., Yagi, C., Hatsuzawa, K., Katoh, Y., Shin, H.-W., Takahashi, S. and Nakayama, K. (2015). SNAP23/25 and VAMP2 mediate exocytic event of transferrin receptor-containing recycling vesicles. *Biology Open* **4**, 910–920. doi:10.1242/bio.012146
- Linder, S. (2015). MT1-MMP: Endosomal delivery drives breast cancer metastasis. *J. Cell Biol.* **211**, 215–217. doi:10.1083/jcb.201510009
- Lord, S. J., Velle, K. B., Mullins, R. D. and Fritz-Laylin, L. K. (2020). SuperPlots: Communicating reproducibility and variability in cell biology. *J. Cell Biol.* **219**, e202001064. doi:10.1083/JCB.202001064
- Mader, C. C., Oser, M., Magalhaes, M. A. O., Bravo-Cordero, J. J., Condeelis, J., Koleske, A. J. and Gil-Henn, H. (2011). An EGFR-Src-Arg-cortactin pathway mediates functional maturation of invadopodia and breast cancer cell invasion. *Cancer Res.* **71**, 1730–1741. doi:10.1158/0008-5472.CAN-10-1432
- Miyagawa, T., Hasegawa, K., Aoki, Y., Watanabe, T., Otagiri, Y., Arasaki, K., Wakana, Y., Asano, K., Tanaka, M., Yamaguchi, H. et al. (2019). MT1-MMP recruits the ER-Golgi SNARE Bet1 for efficient MT1-MMP transport to the plasmamembrane. *J. Cell Biol.* **218**, 3355–3371. doi:10.1083/jcb.201808149
- Miyata, T., Ohnishi, H., Suzuki, J., Yoshikumi, Y., Ohno, H., Mashima, H., Yasuda, H., Ishijima, T., Osawa, H., Satoh, K. et al. (2004). Involvement of syntaxin 4 in the transport of membrane-type 1 matrix metalloproteinase to the plasma membrane in human gastric epithelial cells. *Biochem. Biophys. Res. Commun.* **323**, 118–124. doi:10.1016/j.bbrc.2004.08.064
- Mori, Y., Takenaka, K., Fukazawa, Y. and Takamori, S. (2021). The endosomal Q-SNARE, Syntaxin 7, defines a rapidly replenishing synaptic vesicle recycling pool in hippocampal neurons. *Commun. Biol.* **4**, 981. doi:10.1038/s42003-021-02512-4
- Mukherjee, M., Chow, S. Y., Yusoff, P., Seetharaman, J., Ng, C., Sinniah, S., Koh, X. W., Asgar, N. F. M., Li, D., Yim, D. et al. (2012). Structure of a novel phosphotyrosine-binding domain in Hakai that targets E-cadherin. *EMBO J.* **31**, 1308–1319. doi:10.1038/emboj.2011.496
- Mullock, B. M., Smith, C. W., Ihrke, G., Bright, N. A., Lindsay, M., Parkinson, E. J., Brooks, D. A., Parton, R. G., James, D. E., Luzio, J. P. et al. (2000). Syntaxin 7 is localized to late endosome compartments, associates with Vamp 8, and is required for late endosome-lysosome fusion. *Mol. Biol. Cell* **11**, 3137–3153. doi:10.1091/mbc.11.9.3137
- Murphy, D. A. and Courtneidge, S. A. (2011). The “ins” and “outs” of podosomes and invadopodia: Characteristics, formation and function. *Nat. Rev. Mol. Cell Biol.* **12**, 413–426. doi:10.1038/nrm3141
- Nakamura, N., Yamamoto, A., Wada, Y. and Futai, M. (2000). Syntaxin 7 mediates endocytic trafficking to late endosomes. *J. Biol. Chem.* **275**, 6523–6529. doi:10.1074/jbc.275.9.6523
- Oser, M., Yamaguchi, H., Mader, C. C., Bravo-Cordero, J. J., Arias, M., Chen, X., Desmarais, V., Van Rhee, J., Koleske, A. J. and Condeelis, J. (2009). Cortactin regulates cofilin and N-WASP activities to control the stages of invadopodium assembly and maturation. *J. Cell Biol.* **186**, 571–587. doi:10.1083/jcb.200812176
- Poincloux, R., Lizárraga, F. and Chavrier, P. (2009). Matrix invasion by tumour cells: a focus on MT1-MMP trafficking to invadopodia. *J. Cell Sci.* **122**, 3015–3024. doi:10.1242/jcs.034561
- Prekeris, R., Yang, B., Oorschot, V., Klumperman, J. and Bonifacio, J. (1999). Differential roles of syntaxin 7 and syntaxin 8 in endosomal trafficking. *Mol. Biol. Cell* **10**, 3891–3908. doi:10.1091/mbc.10.11.3891
- Priya, A., Kalaidzidis, I. V., Kalaidzidis, Y., Lambright, D. and Datta, S. (2015). Molecular insights into Rab7-mediated endosomal recruitment of core retromer: deciphering the role of Vps26 and Vps35. *Traffic* **16**, 68–84. doi:10.1111/tra.12237
- Pryor, P. R., Mullock, B. M., Bright, N. A., Lindsay, M. R., Gray, S. R., Richardson, S. C. W., Stewart, A., James, D. E., Piper, R. C. and Luzio, J. P. (2004). Combinatorial SNARE complexes with VAMP7 or VAMP8 define different

- late endocytic fusion events. *EMBO Rep.* **5**, 590-595. doi:10.1038/sj.embor.7400150
- Qiang, L., Cao, H., Chen, J., Weller, S. G., Krueger, E. W., Zhang, L., Razidlo, G. L. and Mcniven, M. A. (2019). Pancreatic tumor cell metastasis is restricted by MT1-MMP binding protein MTCBP-1. *J. Cell Biol.* **218**, 317-332. doi:10.1083/jcb.201802032
- Remacle, A., Murphy, G. and Roghi, C. (2003). Membrane type 1-matrix metalloproteinase (MT1-MMP) is internalised by two different pathways and is recycled to the cell surface. *J. Cell Sci.* **116**, 3905-3916. doi:10.1242/jcs.00710
- Rink, J., Ghigo, E., Kalaidzidis, Y. and Zerial, M. (2005). Rab conversion as a mechanism of progression from early to late endosomes. *Cell* **122**, 735-749. doi:10.1016/j.cell.2005.06.043
- Rosenberg, B. J., Gil-Henn, H., Mader, C. C., Halo, T., Yin, T., Condeelis, J., Machida, K., Wu, Y. I. and Forscher, P. (2017). Phosphorylated cortactin recruits Vav2 guanine nucleotide exchange factor to activate Rac3 and promote invadopodial function in invasive breast cancer cells. *Mol. Biol. Cell* **28**, 1347-1360. doi:10.1091/mbc.e16-12-0885
- Rothbauer, U., Zolghadr, K., Tillib, S., Nowak, D., Schermelleh, L., Gahl, A., Backmann, N., Conrath, K., Muyldermans, S., Cardoso, M. C. et al. (2006). Targeting and tracing antigens in live cells with fluorescent nanobodies. *Nat. Methods* **3**, 887-889. doi:10.1038/nmeth953
- Rothbauer, U., Zolghadr, K., Muyldermans, S., Schepers, A., Cardoso, M. C. and Leonhardt, H. (2008). A versatile nanotrap for biochemical and functional studies with fluorescent fusion proteins. *Mol. Cell. Proteomics : MCP* **7**, 282-289. doi:10.1074/mcp.M700342-MCP200
- Sangrar, W., Gao, Y., Scott, M., Truesdell, P. and Greer, P. A. (2007). Ferment-mediated cortactin phosphorylation is associated with efficient fibroblast migration and is dependent on reactive oxygen species generation during integrin-mediated cell adhesion. *Mol. Cell. Biol.* **27**, 6140-6152. doi:10.1128/MCB.01744-06
- Sharma, P., Parveen, S., Shah, L. V., Mukherjee, M., Kalaidzidis, Y., Kozielski, A. J., Rosato, R., Chang, J. C. and Datta, S. (2020). SNX27-retromer assembly recycles MT1-MMP to invadopodia and promotes breast cancer metastasis. *J. Cell Biol.* **219**, e201812098. doi:10.1083/jcb.201812098
- Sneeggen, M., Pedersen, N. M., Campsteijn, C., Haugsten, E. M., Stenmark, H. and Schink, K. O. (2019). WDFY2 restrains matrix metalloproteinase secretion and cell invasion by controlling VAMP3-dependent recycling. *Nat. Commun.* **10**, 2850. doi:10.1038/s41467-019-10794-w
- Steffen, A., Le Dez, G., Poincloux, R., Recchi, C., Nassoy, P., Rottner, K., Galli, T. and Chavrier, P. (2008). MT1-MMP-dependent invasion is regulated by TI-VAMP/VAMP7. *Curr. Biol.* **18**, 926-931. doi:10.1016/j.cub.2008.05.044
- Stetler-Stevenson, W. G. (2001). The role of matrix metalloproteinases in tumor invasion, metastasis, and angiogenesis. *Surg. Oncol. Clin. N Am.* **10**, 383-392. doi:10.1016/S1055-3207(18)30071-1
- Südhof, T. C. and Rothman, J. E. (2009). *Membrane Fusion: Grappling with SNARE and SM Proteins* Downloaded from. Available at: <http://science.sciencemag.org/>.
- Suzuki, J., Ohnishi, H., Wada, A., Hirayama, T., Ohno, H., Ueda, N., Yasuda, H., Iiri, T., Wada, Y., Futai, M. et al. (2003). Involvement of syntaxin 7 in human gastric epithelial cell vacuolation induced by the *Helicobacter pylori*-produced cytotoxin VacA. *J. Biol. Chem.* **278**, 25585-25590. doi:10.1074/jbc.M212445200
- Tang, J. C. Y., Szikra, T., Kozorovitskiy, Y., Teixeira, M., Sabatini, B. L., Roska, B. and Cepko, C. L. (2013). A nanobody-based system using fluorescent proteins as scaffolds for cell-specific gene manipulation. *Cell* **154**, 928-939. doi:10.1016/j.cell.2013.07.021
- Wang, G., Nola, S., Bovio, S., Bun, P., Coppey-Moisand, M., Lafont, F. and Galli, T. (2018). Biomechanical control of lysosomal secretion Via the VAMP7 Hub: a tug-of-war between VARP and LRRK1. *iScience* **4**, 127-143. doi:10.1016/j.isci.2018.05.016
- Wang, G. and Galli, T. (2018). Reciprocal link between cell biomechanics and exocytosis. *Traffic* **19**, 741-749. doi:10.1111/tra.12584
- Ward, D. M., Pevsner, J., Scullion, M. A., Vaughn, M. and Pfeffer, S. R. (2000). Syntaxin 7 and VAMP-7 are soluble N-Ethylmaleimide-sensitive factor attachment protein receptors required for late endosome-lysosome and homotypic lysosome fusion in alveolar macrophages. *Mol. Biol. Cell* **11**, 2327-2333. doi:10.1091/mbc.11.7.2327
- Weidmann, M. D., Surve, C. R., Eddy, R. J., Chen, X., Gertler, F. B., Sharma, V. P. and Condeelis, J. S. (2016). Mena(INV) dysregulates cortactin phosphorylation to promote invadopodium maturation. *Sci. Rep.* **6**, 36142. doi:10.1038/srep36142
- West, Z. E., Aitchison, S. M., Semmler, A. B. T. and Murray, R. Z. (2021). The trans-SNARE complex VAMP4/Stx6/Stx7/Vti1b is a key regulator of Golgi to late endosome MT1-MMP transport in macrophages. *Traffic* **22**, 368-376. doi:10.1111/tra.12813
- Wienands, J., Larbolette, O. and Reth, M. (1996). Evidence for a preformed transducer complex organized by the B cell antigen receptor. *Proc. Natl. Acad. Sci. U.S.A.* **93**, 7865-7870. doi:10.1073/pnas.93.15.7865
- Williams, K. C., Mcneilly, R. E. and Coppolino, M. G. (2014). SNAP23, Syntaxin4, and vesicle-associated membrane protein 7 (VAMP7) mediate trafficking of membrane type 1-matrix metalloproteinase (MT1-MMP) during invadopodium formation and tumor cell invasion. *Mol. Biol. Cell* **25**, 2061-2070. doi:10.1091/mbc.e13-10-0582
- Wolf, K., Wu, Y. I., Liu, Y., Geiger, J., Tam, E., Overall, C., Stack, M. S. and Friedl, P. (2007). Multi-step pericellular proteolysis controls the transition from individual to collective cancer cell invasion. *Nat. Cell Biol.* **9**, 893-904. doi:10.1038/ncb1616
- Yamaguchi, H., Takeo, Y., Yoshida, S., Kouchi, Z., Nakamura, Y. and Fukami, K. (2009). Lipid rafts and caveolin-1 are required for invadopodia formation and extracellular matrix degradation by human breast cancer cells. *Cancer Res.* **69**, 8594-8602. doi:10.1158/0008-5472.CAN-09-2305
- Zagryazhskaya-Masson, A., Monteiro, P., Macé, A.-S., Castagnino, A., Ferrari, R., Infante, E., Duperray-Susini, A., Dingli, F., Lanyi, A., Loew, D. et al. (2020). Intersection of TKS5 and FGD1/CDC42 signaling cascades directs the formation of invadopodia. *J. Cell Biol.* **219**, e201910132. doi:10.1083/jcb.201910132
- Zhao, J., Wei, J., Mialki, R., Zou, C., Mallampalli, R. K. and Zhao, Y. (2012). Extracellular signal-regulated kinase (ERK) regulates cortactin ubiquitination and degradation in lung epithelial cells. *J. Biol. Chem.* **287**, 19105-19114. doi:10.1074/jbc.M112.339507
- Zhu, D., Xie, L., Kang, Y., Dolai, S., Bondo Hansen, J., Qin, T., Xie, H., Liang, T., Rubin, D. C., Osborne, L. et al. (2017). Syntaxin 2 acts as inhibitory snare for insulin granule exocytosis. *Diabetes* **66**, 948-959. doi:10.2337/db16-0636

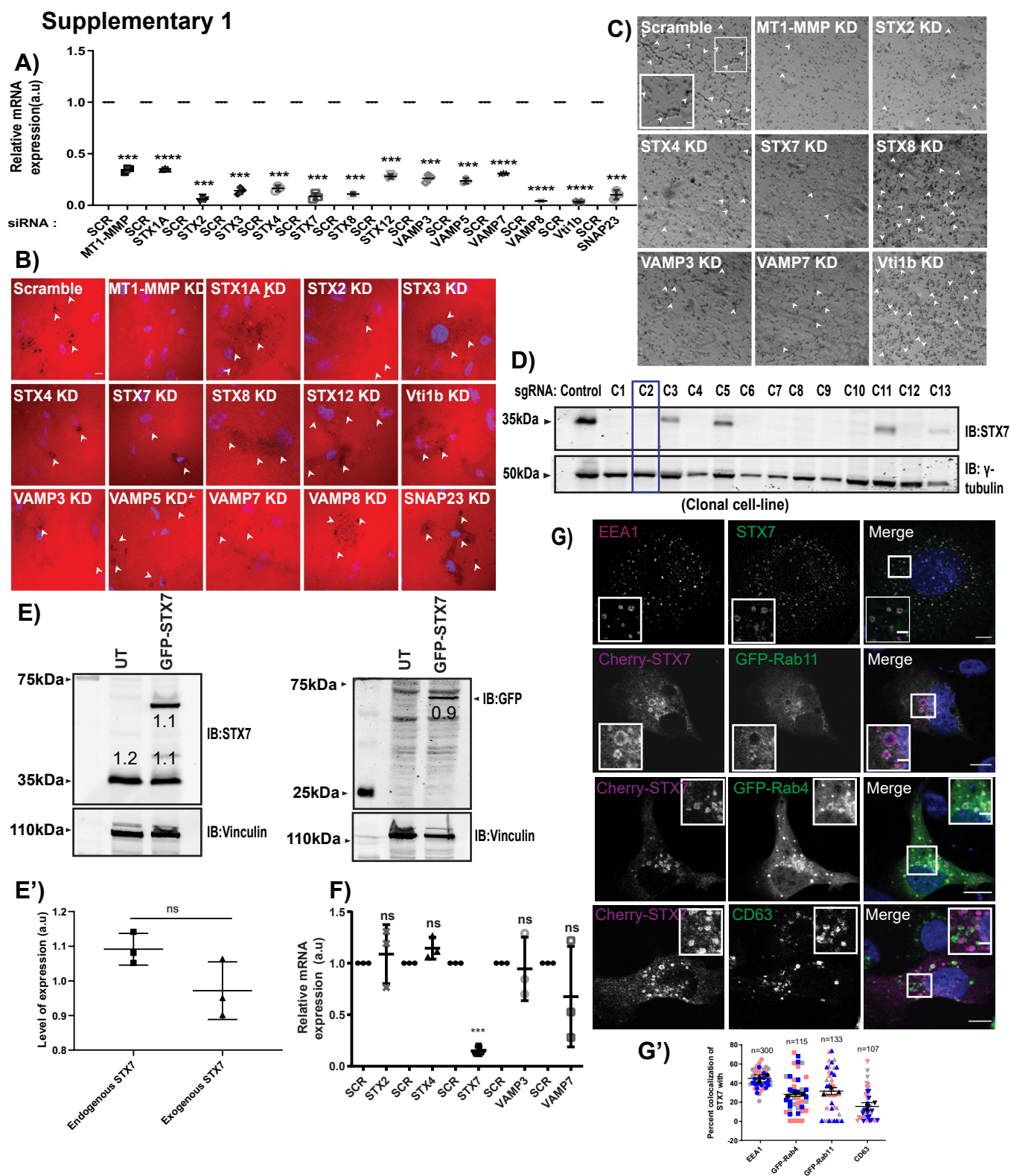


Fig. S1. Screening of SNAREs of endocytic and recycling pathway. A) Indicated SNAREs were depleted using siRNA in MDA-MB-231. The efficacy of gene suppression was quantified using qPCR. (N=3). Two-tailed Student's t test, *** $P < 0.001$, **** $P < 0.0001$. B) Indicated molecules were depleted using siRNA in MDA-MB-231. Post-transfection cells were seeded on Alexa Fluor 568 labeled gelatin-coated coverslip for 12h. Arrowhead indicates the degradation spot. (N=3, n=300 cells, Scale bar 10 μm). C) Indicated molecules were depleted using siRNA in MDA-MB-231. Post-transfection, cells were seeded on Matrigel-coated cell inserts for 20h. Arrowhead indicates the cells that invaded through the Matrigel. (N=3, n=50,000 cells, Scale bar 10 μm). D) Different clones of MDA-MB-231 STX7KO clonal cells (STX7KO) were obtained after cells were transfected with Cas9 protein complexes with either control sgRNA or sgRNA-targeting STX7. The knockout efficiency was determined by immunoblotting using anti-STX7 and anti- γ -Tubulin (loading control). The boxed region indicates the clone used in the study. E and E') UT and GFP-STX7 transfected MDA-MB-231 cells were lysed and proceed for immunoblotting using anti-STX7, anti-vinculin and anti-GFP. Anti-Vinculin was used as a loading control. The level of expression of GFP-STX7 (exogenous) compared to endogenous STX7 was quantified and plotted. Two-tailed Student's t-test, $P > 0.05$ -ns (non-significant). F) STX7 was depleted using siRNA in MDA-MB-231, and the relative expression of indicated SNARE molecules were checked via qPCR (N=3). Two-tailed Student's t test, *** $P < 0.001$, ns-non significant. G and G') MDA-MB-231 cells were immunostained with EEA1/STX7, co-expressed with Cherry-STX7 and GFP-Rab11 or GFP-Rab4 and Cherry-STX7/CD63. Inset represents the zoomed-in view of the boxed region. Percentage co-localization of STX7 with respective compartments was quantified and plotted (N=3, Scale bar 10 μm , inset 3 μm). The data are displayed using SuperPlots, each biological replicate is distinctly color-coded and each dot represents identified percentage colocalization in a field of view (frame), described in the Material and methods. All the graphs represent means \pm SD. N- number of experimental repeats, n- number of cells analyzed.

Supplementary 2

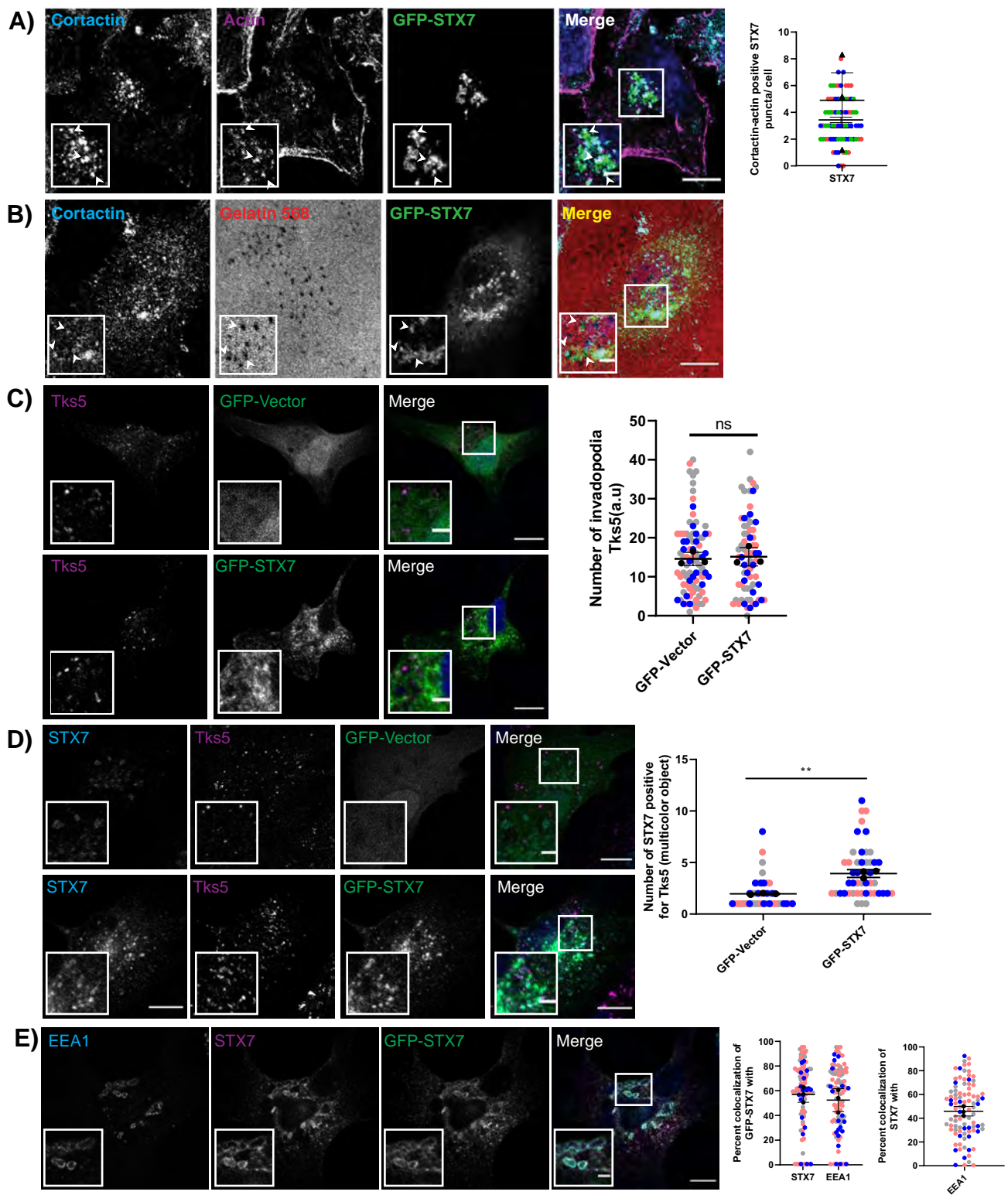


Fig. S2. STX7 is invadopodia associated. A) GFP-STX7 transfected MDA-MB-231 cells were plated over gelatin-coated coverslip and immunostained with cortactin followed by labeling with Phalloidin-568 (F-actin) and DAPI. Inset represents zoomed in view of the boxed region. Arrowhead indicates STX7-Cortactin-actin positive punctae. Graph shows STX7 punctae positive for Cortactin and actin per cell. (N=3, n=77, Scale bar 10µm, Inset 3 µm). B) GFP-STX7 transfected MDA-MB-231 cells were plated over Alexa fluor 568 labeled gelatin-coated coverslip for 12h, followed by immuno-staining with cortactin. DAPI was used to label the nucleus. Inset represents zoomed-in view of the boxed region. Arrowhead indicates STX7 localization near degradation spot (N=2, n=40. Scale bar 10µm, Inset 3 µm). C) GFP-Vector and GFP-STX7 transfected MDA-MB-231 cells were seeded on the unlabelled gelatin-coated coverslip, immunostained with Tks5 followed by labelling with DAPI. Inset represents zoomed in view of the boxed region. Number of Tks5 punctae were counted and plotted. {N=3, n=84(GFP-Vector), n=70(GFP-STX7), Scale bar 10µm, Inset 3 µm}. Two-tailed Student's t-test, $P > 0.05$ - ns (non-significant). D) GFP-Vector and GFP-STX7 transfected MDA-MB-231 cells were seeded on the unlabelled gelatin-coated coverslip, immunostained with Tks5, STX7 followed by DAPI staining. Inset represents zoomed in view of the boxed region. Number of STX7 and Tks5 punctae were counted and plotted. {N=3, n=42(GFP-Vector), n=47(GFP-STX7), Scale bar 10µm, Inset 3 µm}. Two-tailed Student's t-test, $** P < 0.01$. E) GFP-STX7 transfected MDA-MB-231 cells were immunostained using STX7 and EEA1. Inset represents zoomed in view of the boxed region. Graph represents the percent colocalisation of GFP-STX7 with STX7 or EEA1. (N=3, n=94, Scale bar 10µm, Inset 3 µm). The data that are displayed using SuperPlots, each biological replicate is distinctly color-coded and each dot represents identified multicolor objects/percentage colocalization in a field of view (frame), described in the Material and methods. All the graphs represent means \pm SD. N- number of experimental repeats, n- number of cells analyzed.

Supplementary 3

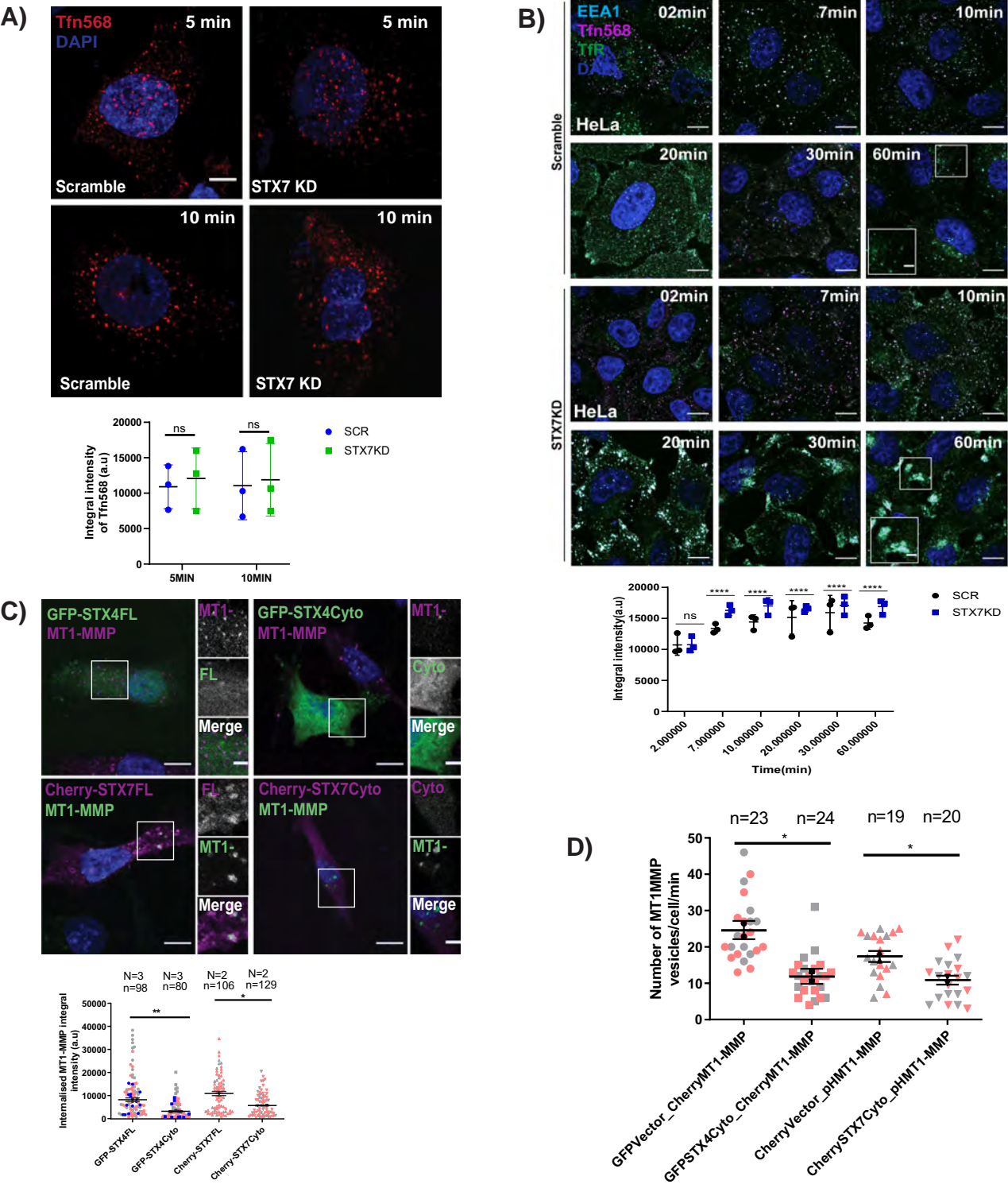


Fig. S3. STX7 is involved in recycling but not endocytosis. A) Control siRNA and STX7 depleted MDA-MB-231 cells were serum-starved and incubated with Alexa Fluor 568 labeled transferrin for 1h at 4°C. Cells were shifted to 37 °C to chase the bound cargo for 5 and 10min. Cells were fixed and stained with DAPI to label the nucleus. Integral intensity of the endocytosed transferrin was measured and plotted. (N=3, n≥300, Scale bar 10 μm). Two-tailed Student's t test, P>0.05, ns-non significant. B) HeLa cells were treated as mentioned above, and the bound cargo was chased for 2-60min. Cells were immunostained with EEA1 and Transferrin receptor (TfR). Inset represents the zoomed-in view of the boxed region. Integral intensity of the labeled Tfn-568 with due course of time was calculated and plotted. (N=3, n≥300 cells, Scale bar 10 μm, inset 3 μm), One way ANOVA, **** P < 0.0001, P>0.05-ns-non significant. C) MDA-MB-231 cells were transfected with GFP-STX4FL/Cyto and Cherry-STX7FL/Cyto. Post- transfection cells were incubated with antibodies against MT1-MMP at 4°C for 1h, then shifted to 37°C for 15 min. Cells were fixed, stained with DAPI to label the nucleus, and imaged with a confocal microscope. The insets represent the zoomed-in view of the boxed region showing the MT1-MMP antibody uptake by the cells. The observed signal corresponds to internalized anti-MT1-MMP antibody (Scale bars = 10 μm, inset = 3 μm). Two-tailed Student's t-test, * < 0.05, ** P < 0.01. D) MDA-MB-231 cells were co-expressed with GFP-Vector/ChMT1-MMP, GFP-STX4Cyto/Cherry-MT1-MMP, Cherry-Vector/pHMT1-MMP and Cherry-STX7Cyto/pHMT1-MMP. Cells were allowed to adhere to the gelatin-coated imaging dishes for 6h and then subjected to TIRF microscopy. The number of MT1-MMP vesicles that are available in the TIRF plane and could form a track spanning minimum 4 consecutive frames captured over 1 minute duration was quantified and plotted {N = 2, n=23(GFP-Vector_ChMT1-MMP), n=24(GFP-STX4Cyto_ChMT1-MMP), n=20(Cherry-Vector_pHMT1-MMP), n=20(Cherry-STX7Cyto_pHMT1-MMP)}. Two-tailed Student's t test, * < 0.05. See Materials and methods for details. The data that are displayed using SuperPlots, each biological replicate is distinctly color-coded and each dot represents identified objects/integral intensity in a field of view (frame), described in the Material and methods. All the graphs represent means ± SD. N- number of experimental repeats, n- number of cells analyzed.

Supplementary 4

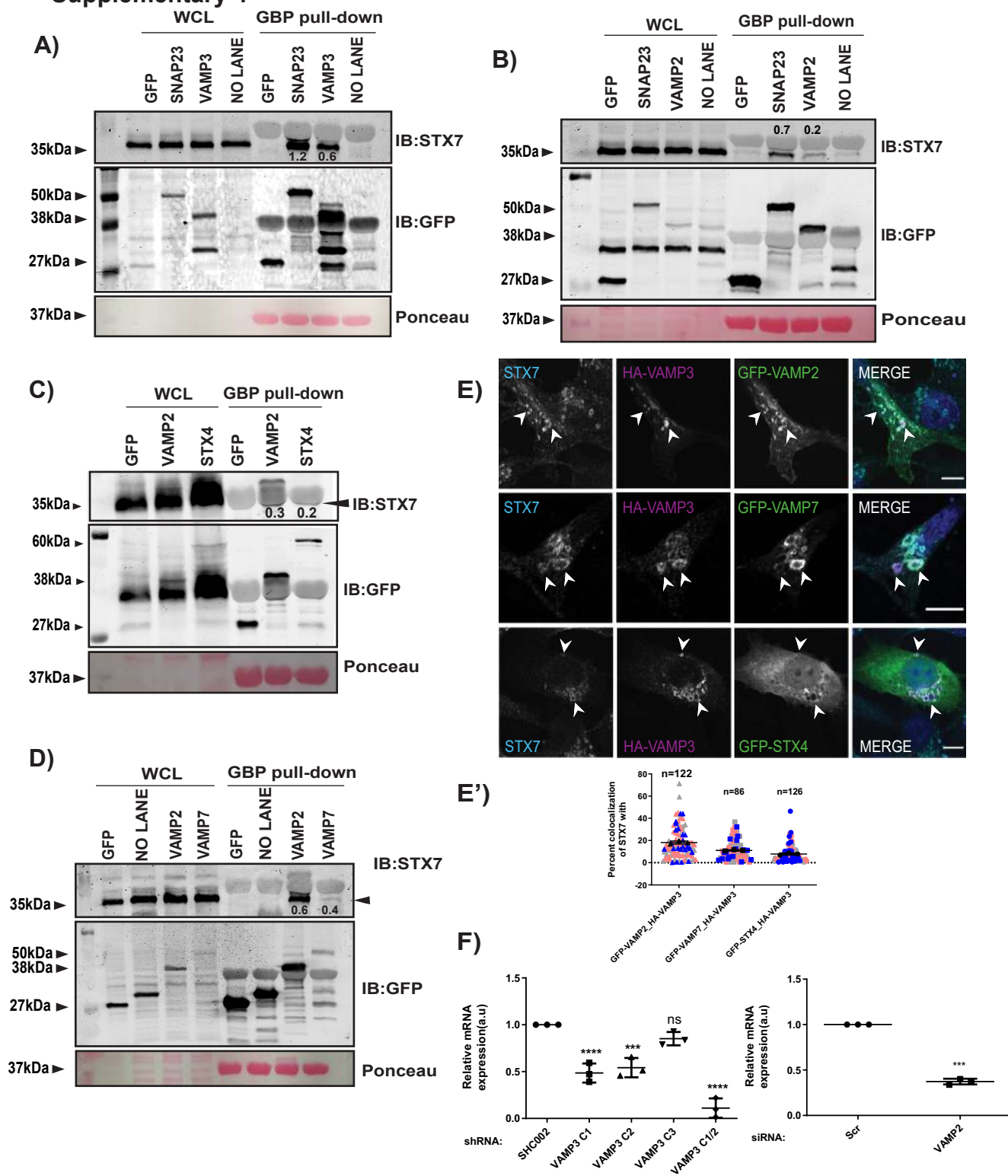
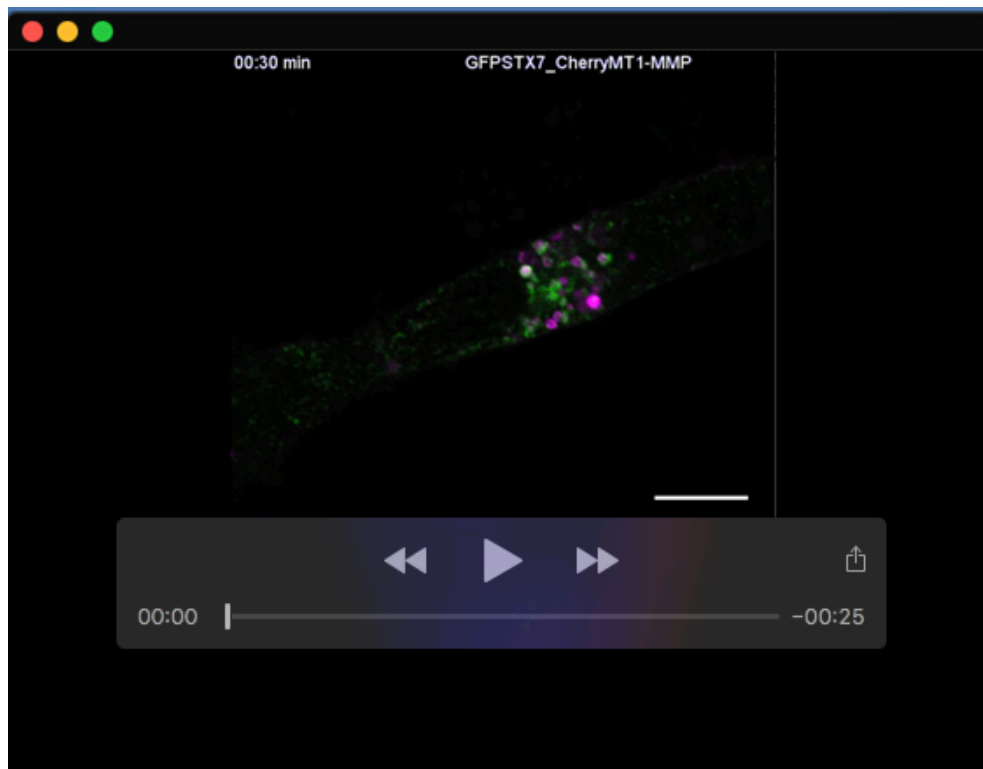
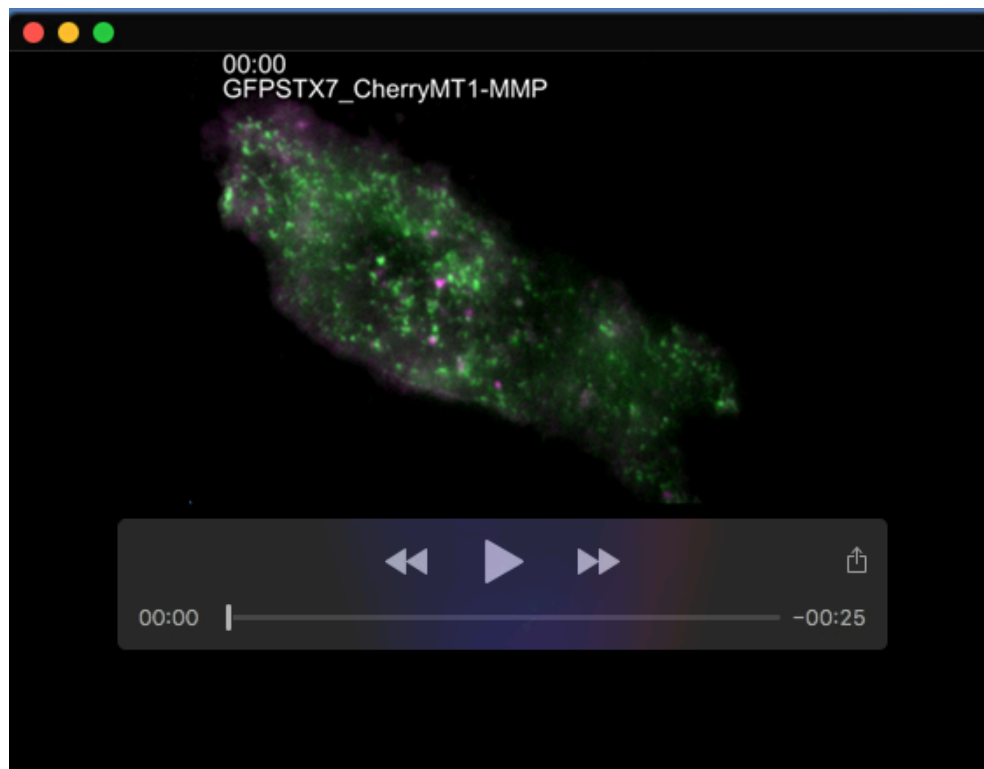


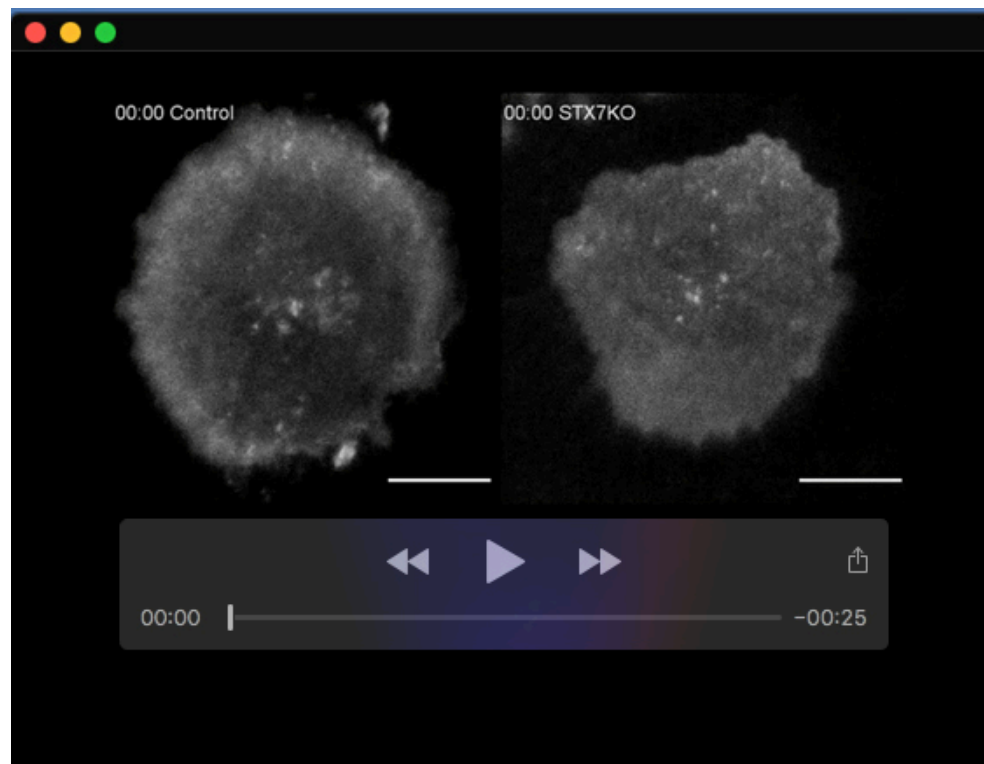
Fig. S4. A and B) GBP pull-down was performed with lysates from MDA-MB-231 cells expressing GFP- vector, GFP- tagged SNAP23, VAMP3 and VAMP2, pre-treated with 1mM NEM. Purified GST–GBP (25µg) was incubated with glutathione sepharose beads and allowed to bind with the respective lysates (300µg) for 5h. Beads were washed, boiled, and advanced for immunoblotting sequentially using anti-STX7, anti-GFP antibodies. The number represents the normalized value of prey protein (STX7) with respect to the precipitated protein (GFP-tagged protein). C and D) GBP pull-down was performed with lysates from HEK293 cells expressing GFP-Vector, GFP-tagged VAMP2, STX4 and VAMP7, pre-treated with 1mM NEM. Purified GST–GBP (25µg) was incubated with glutathione sepharose beads and allowed to bind with the respective lysates GFP-Vector (300µg), GFP- VAMP2 (300µg), GFP- STX4 (900µg) and GFP- VAMP7 (900µg) for 5h. Beads were washed, boiled, and advanced for immunoblotting sequentially using anti-STX7, anti-GFP antibodies. The number represents the normalized value of prey protein (STX7) with respect to the precipitated protein (GFP-tagged protein). Black arrowhead indicates the band of interest. E and E') MDA-MB-231 cells were independently co-expressed with HA-VAMP3 and GFP-VAMP2/GFP-VAMP7/GFP-STX4, fixed using 4% PFA, immunostained with STX7, and labeled with DAPI to label the nucleus. The percentage of co-localization was quantified and plotted. Arrowhead indicates the colocalized objects. {N=3, n=122 (GFP-VAMP2_HA-VAMP3), n=86 (GFP-VAMP7_HA-VAMP3), n=126(GFP-STX4_HA-VAMP3); Scale bar 10 µm}. The data is displayed using SuperPlots, each biological replicate is distinctly color-coded and each dot represents identified multicolor objects/percentage colocalization in a field of view (frame), described in the Material and methods. F) Gene silencing efficiency of VAMP3 and VAMP2 in MDA-MB-231 was detected by qPCR (N=3), One way ANOVA, *** $P < 0.001$, **** $P < 0.0001$, ns-non-significant. N- number of experimental repeats, n- number of cells analyzed. The graph represents means±SD.



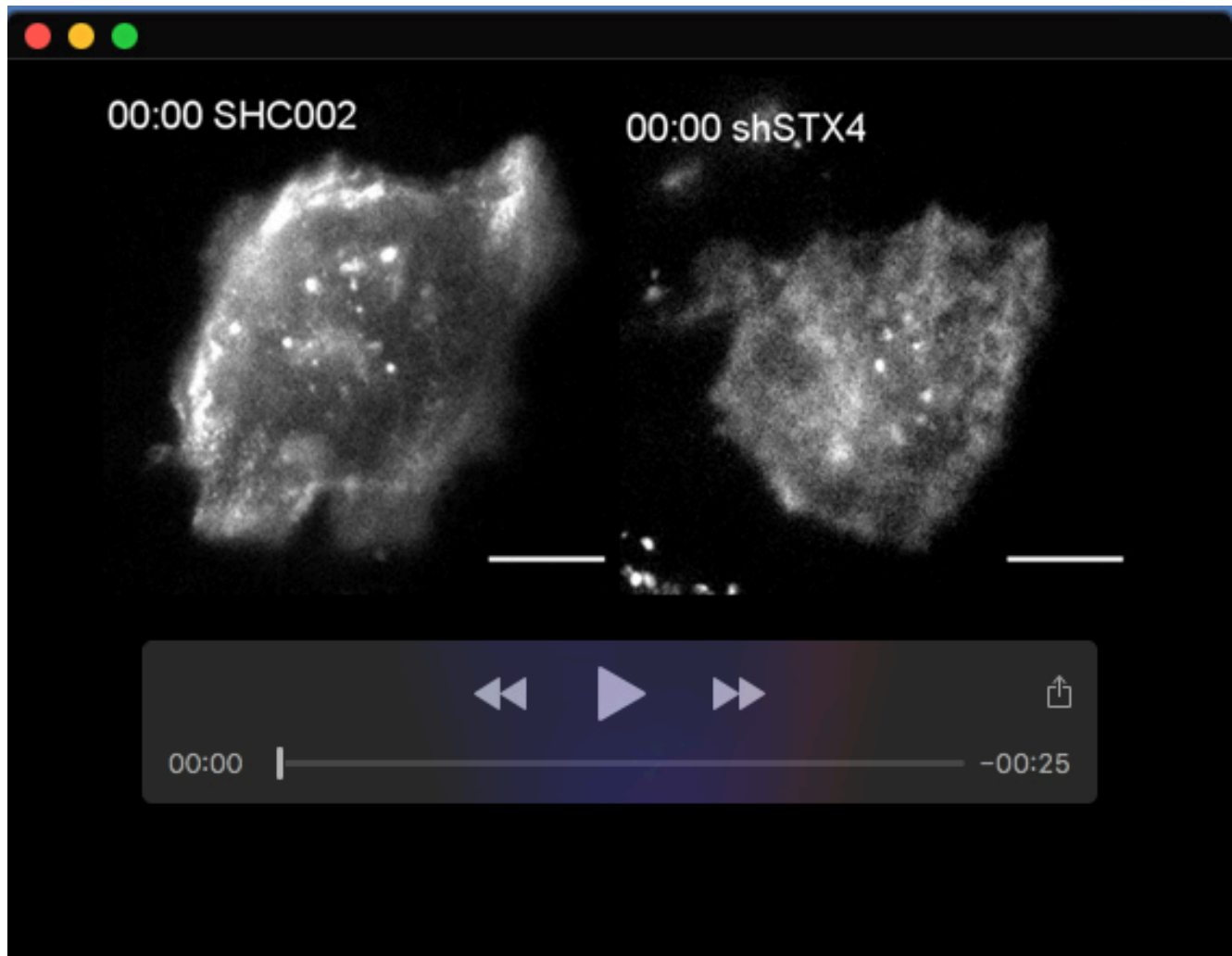
Movie 1. MDA-MB-231 cells cotransfected with Cherry-MT1-MMP and GFP-STX7. Cells were analyzed using a live-cell confocal microscope (Fig. 2E). Scale bar 10 μm , Inset 3 μm . Exposure time: 4.0 μs /pixel.



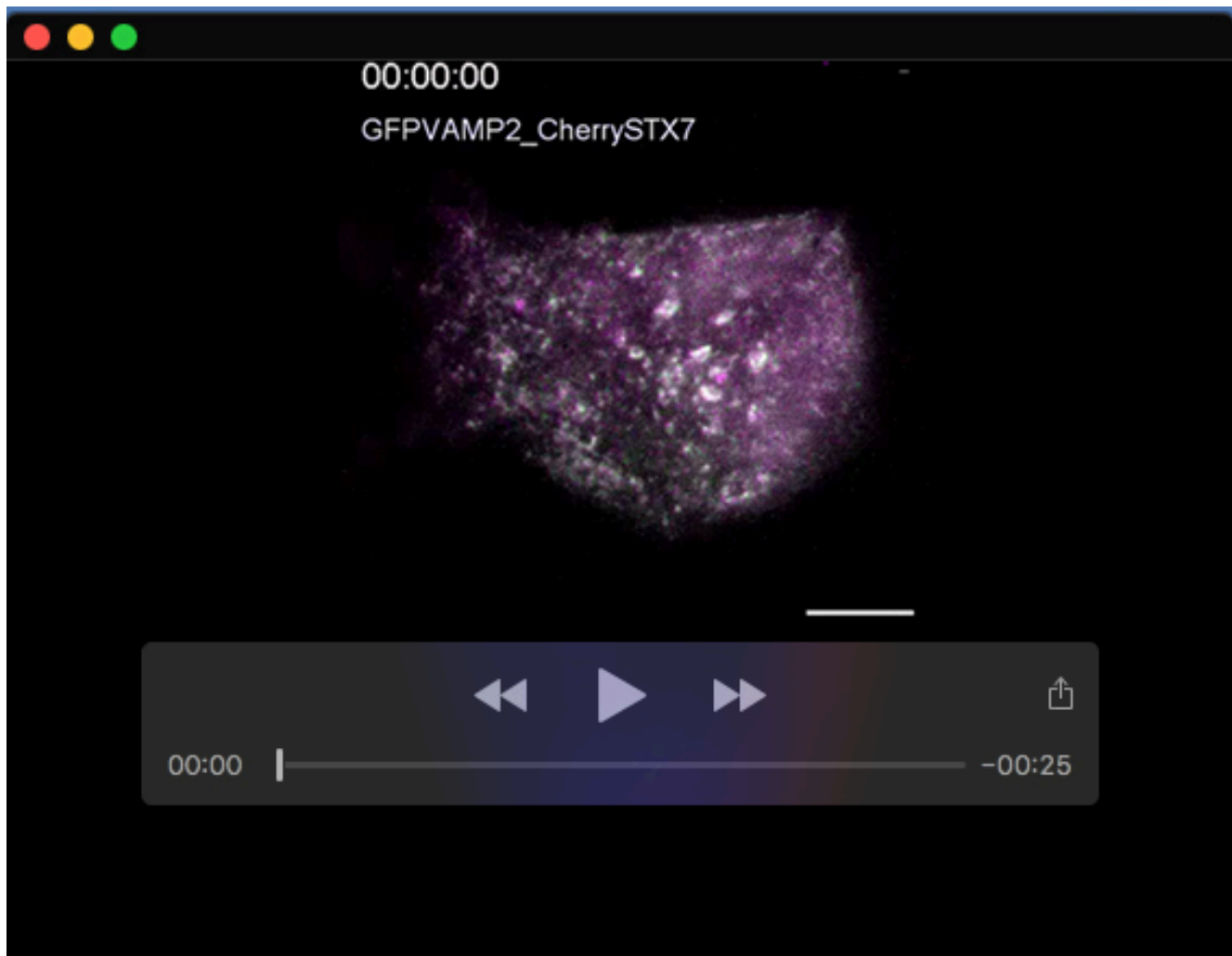
Movie 2. MD A-MB-231 cells cotransfected with Cherry-MT1-MMP and GFP-STX7. Cells were plated on a gelatin-coated imaging dish, and videos were captured using a TIRF microscope (Fig. 3A). Scale bar 10 μ m. Exposure time, TIRF Red: 800ms, TIRF Green: 500ms.



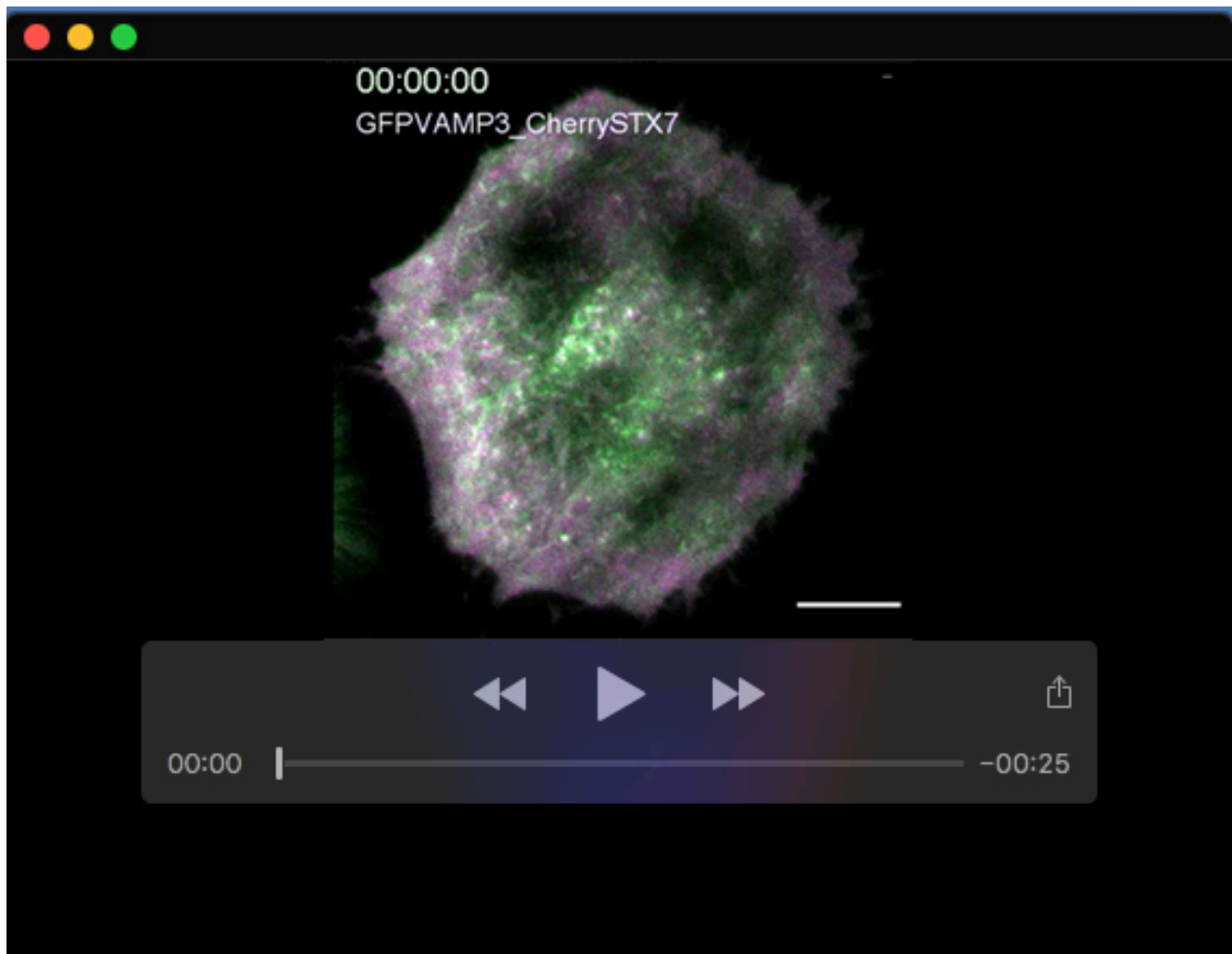
Movie 3. MDA-MB-231 control and STX7KO clonal cells (STX7KO) were transfected with pHluorinMT1-MMP. Cells were plated on a gelatin-coated imaging dish, and videos were captured using a TIRF microscope (Fig. 3A). Scale bar 10 μ m. Exposure time, TIRF Green: 600ms (Control); 800ms (STX7KO).



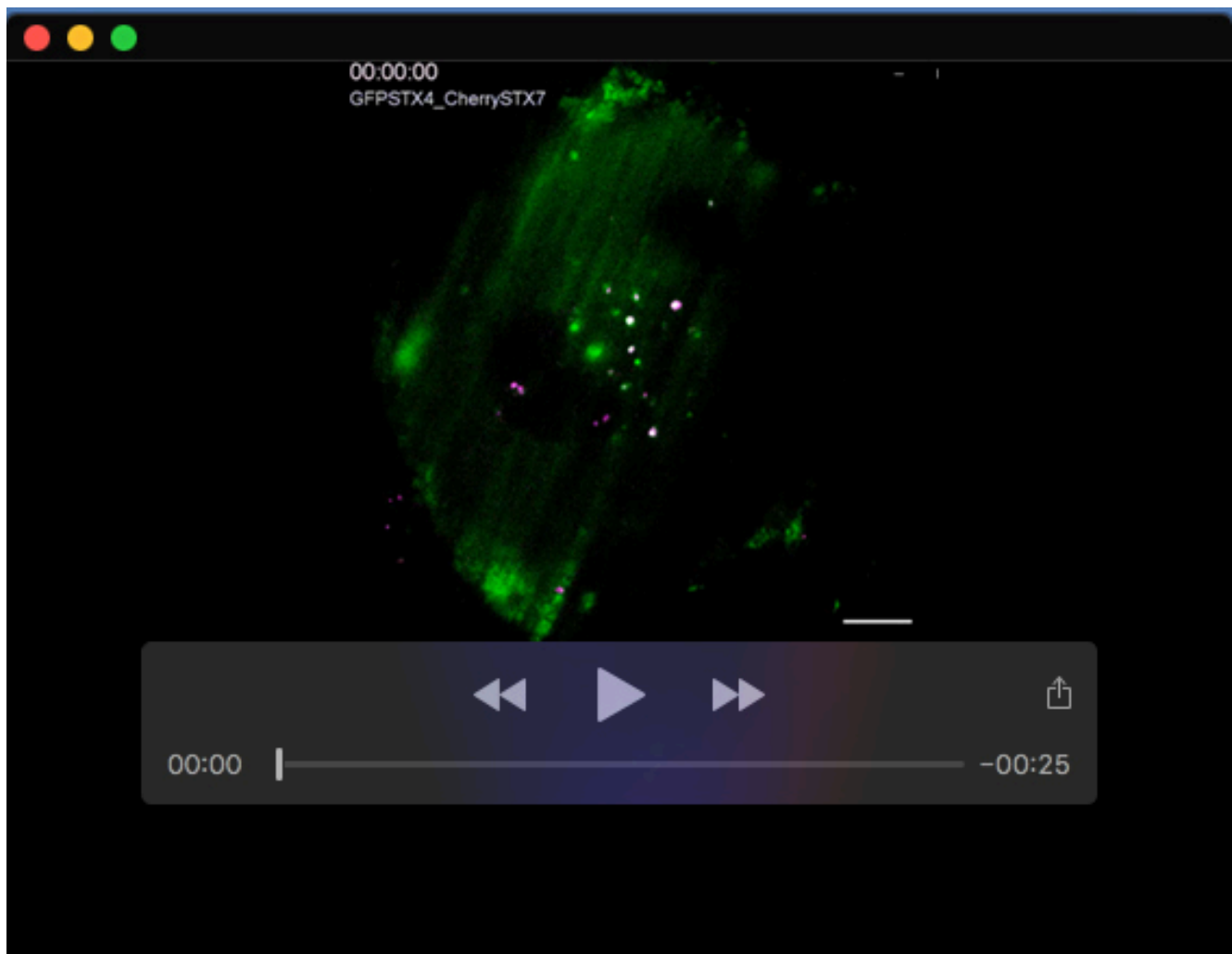
Movie 4. MDA-MB-231 cells were transfected with SHC002 and shSTX4. Depleted cells were transfected with pHluorinMT1-MMP. Cells were plated on a gelatin-coated imaging dish, and videos were captured using a TIRF microscope (Fig. 3A). Scale bar 10 μ m. Exposure time, TIRF Green: 400ms (SHC002); 500ms (shSTX4).



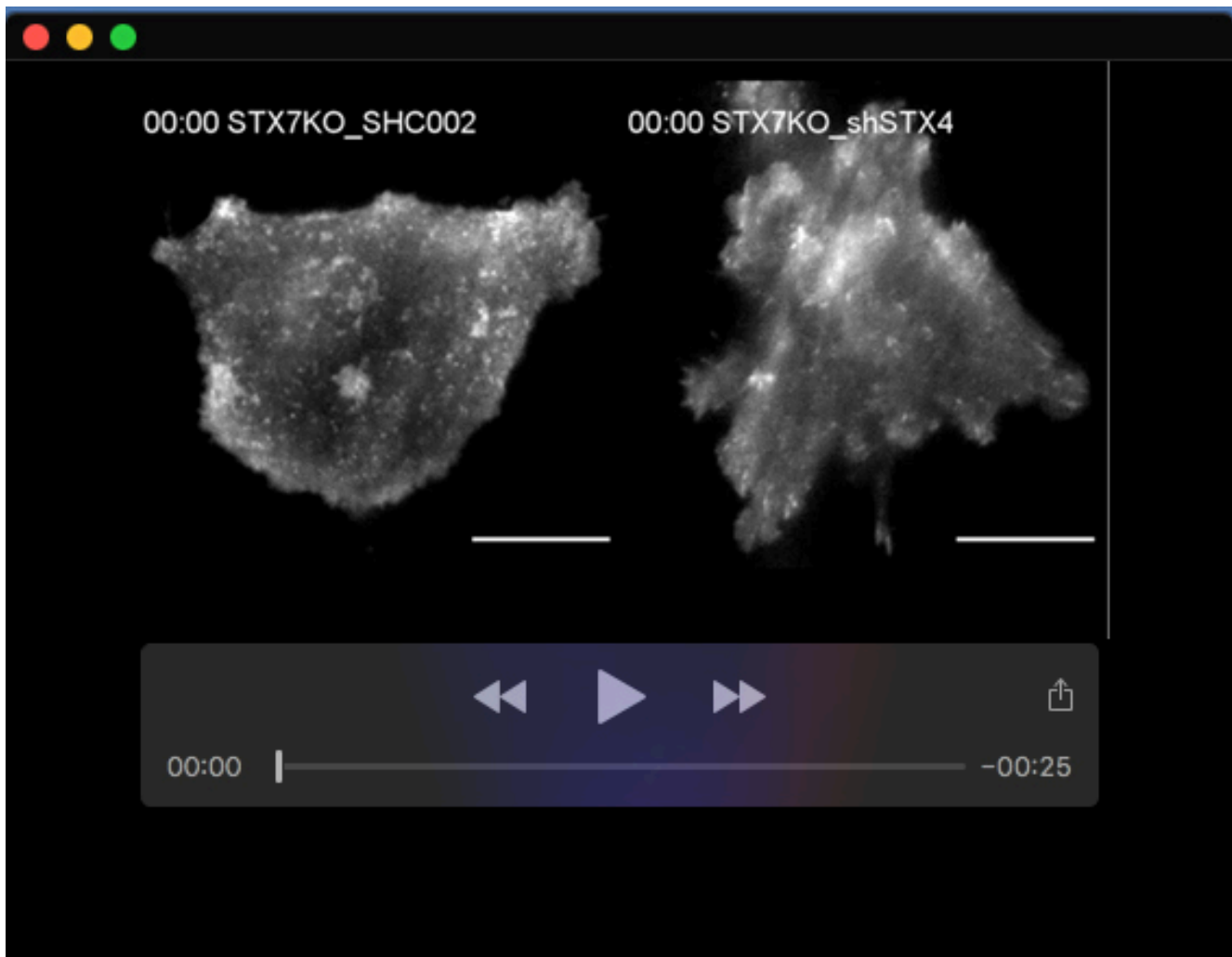
Movie 5. MDA-MB-231 cells cotransfected with Cherry-STX7 and GFP-VAMP2. Cells were plated on a gelatin-coated imaging dish, and videos were captured using a TIRF microscope (Fig. 4D). Scale bar 10 μ m. Exposure time, TIRF Red: 200ms, TIRF Green: 50ms.



Movie 6. MDA-MB-231 cells cotransfected with Cherry-STX7 and GFP-VAMP3. Cells were plated on a gelatin-coated imaging dish and videos were captured using a TIRF microscope (Fig. 4D). Scale bar 10 μ m. Exposure time, TIRF Red: 100ms, TIRF Green: 100ms.



Movie 7. MDA-MB-231 cells cotransfected with Cherry-STX7 and GFP-STX4. Cells were plated on a gelatin-coated imaging dish, and videos were captured using a TIRF microscope (Fig. 4D). Scale bar 10 μm . Exposure time, TIRF Red: 600ms, TIRF Green: 300ms.



Movie 8. MDA-MB-231 STX7KO clonal cells (STX7KO) were transfected with SHC002 and shSTX4. After 48h of depletion, cells were transfected with pHluorinMT1-MMP. Cells were plated on a gelatin-coated imaging dish, and, videos were captured using a TIRF microscope (Fig. 4I). Scale bar 10 μ m. Exposure time, TIRF Green: 400ms.

Table S1. Oligonucleotide sequences for the siRNA SMARTpool Gene SMARTpool siRNA sequence (5'–3')

Scramble	GGCCAGACGCCCAACCAUA
Scramble	GCGAGCAGCCACCAAUUG
Scramble	GGGAGUACCUGGCGUUUCC
Scramble	CGAACGGCCUGUACGAUGA
MT1MMP	GGAUGGACACGGAGAAUUU
MT1MMP	GGAAACAAGUACUACCGUU
MT1MMP	GGUCUCAAUUGGCAACAUA
MT1MMP	GAUCAAGGCCAAUGUUCGA
STX1A	GGAACACGCGGUAGACUAU
STX1A	AAACAAAGUUCGUUCCAAG
STX1A	GGAGGAGAUUCGAGGCUUC
STX1A	GAGGUGAAGCGGAAGCACA
STX2	UAGACAAGCUCUCAUGAA
STX2	CUUGUGAUCCUUGGAAUUA
STX2	UAGCAACCAUAUCCCAAGA
STX2	GUUAAAGGCUAUUGAACAA
STX3	GAUCAUUGACUCACAGAUU
STX3	AAGAAACUCUACAGUAUCA
STX3	AGGGUGAGAUGUUAGAUAA
STX3	AAACUCGGCUUAACAUUGA
STX4	GGACAAUUCGGCAGACUAU
STX4	GCGUCACAGUGGUUGGAUA
STX4	GCGAGGUGUUUGUGUCCAA
STX4	CGUCAACACAAGAAUGAGA
SNAP23	UAACAGAACUCAACAAUUG
SNAP23	CAACUAAACCGCAUAGAAG
SNAP23	GAAACUCAUUGACAGCUAA
SNAP23	ACAGAGAUCGUAUUGAUUA
VAMP5	UGACGGAAAUUAUGCGUAA

VAMP5	GAUAUGAGCUCAACCUUCA
VAMP5	GAAUAGAGUUGGAGCGGUG
VAMP5	GCAGCAGCGUUCAGACCAA
STX12	CCACAAAUCAGCUCGCCAA
STX12	GAGGAUCAGUAUAUCGGUA
STX12	ACACUACAGUCUCGUAAUA
STX12	GCUCAGAGGUGCACGUCGA
STX7_siRNA#1	GAGUUUGUUGCUCGAGUAA
STX7_siRNA#1	CAGCAGAUUAUCAGCGCAA
STX7_siRNA#1	UGUCAUUGGAGUUGCGAUU
STX7_siRNA#1	GGAGCACACUGUCGCACUA
STX7_siRNA#2	CAAAGAAACAGAUAAAGUAC
STX7_siRNA#2	GCGAUUAUCAGUCUCAUCA
STX7_siRNA#2	GUCAAGGGCAGCAGAUUAU
STX7_siRNA#2	GAGUUUGUUGCUCGAGUAA
STX8	AAUGAAACCAGGCGGGUAA
STX8	GAAUGAGGGUGCCGAACCA
STX8	GAUCUUGUAACUCGAGAGA
STX8	GAGUGAAGAGGCCUAAGCGA
VAMP8	CCACUGGUGCCUUCUCUUA
VAMP8	GUCCUUAUCUGCGUGAUUG
VAMP8	GAAUGAUCGUGUGCGGAA
VAMP8	GGGAAAACUUGGAACAUCU
VTI1B	CCAAAGUAUUGAACGUUCU
VTI1B	GAGCAUAUGAAUCGGCUAC
VTI1B	UGGAGGAGGAGCUACGUUA
VTI1B	UUGCUIAACUCCAUCGGGA
VAMP3	GGAUUACUGUUCUGGUUAU
VAMP3	GAGUUAACGUGGACAAGGU
VAMP3	GGCAGGCGCUUCUCAAUUU
VAMP3	UCAAGUAGAUGAGGUGGUG
VAMP7	GUACUCACAUGGCAAUUAU

VAMP7	GAACGUUCCCGAGCCUUUA
VAMP7	CGAGUUCUCAAGUGUCUUA
VAMP7	GCCAAGACAGGAUUGUAUA
VAMP2	GCGCAAUACUGGUGGAAA
VAMP2	CAUCAUAGUUUACUUCAGC
VAMP2	GGGAGUGAUUUGCGCCAUC
VAMP2	UCAUGAGGGUGAACGUGGA

Table S2. shRNA Information- MISSION shRNA Plasmid DNA Control Vectors

S.No	Name	Sequence
1	SHC002 MISSION pLKO.1-puro Non-Mammalian shRNA Control (TRC1/1.5)_ Non human or mouse shRNA	CCGGCAACAAGATGAAGAGCA CCAACTCGAGTTGGTGCTCTTC ATCTTGTTGTTTTT
2	TRC ID: TRCN0000065023 STX4_AAI44_D10 (Clone1)	CCGGCCGTCAACACAAGAATG AGAACTCGAGTTCTCATTCTTG TGTTGACGGTTTTTG
3	TRC ID: TRCN0000065027 STX4_AAI44_E2 (Clone2)	CCGGGCTGCACGACATATTCA CTTTCTCGAGAAAGTGAATATG TCGTGCAGCTTTTTTG
4	TRC ID: TRCN0000380073 STX4_ LAC36_F12 (Clone3)	GTACCGGGTGACTCGACAGGC CTTAAATCTCGAGATTTAAGGC CTGTCGAGTCACTTTTTTG
5	TRC ID: TRCN0000029814 VAMP3_AAE51_F11 (Clone1)	CCGGCGGGATTACTGTTCTGG TTATCTCGAGATAACCAGAACA GTAATCCCGTTTTT
6	TRC ID: TRCN0000029815 VAMP3_AAE51_F12 (Clone2)	CCGGGCAGCCAAGTTGAAGAG GAAACTCGAGTTTCCTCTTCAA CTTGGCTGCTTTTT
7	TRC ID: TRCN0000029817 VAMP3_AAE51_G2 (Clone3)	CCGGCAGGCGCTTCTCAATTT GAAACTCGAGTTTCAAATTGAG AAGCGCCTGTTTTT

Supplementary 5 : BLOT TRANSPARENCY

Figure 1C' (1)

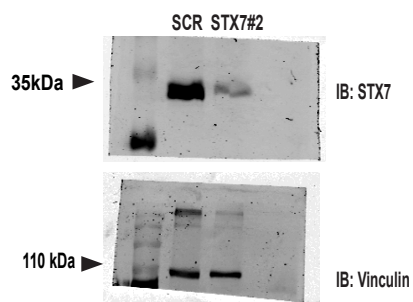


Figure 1C' (2)

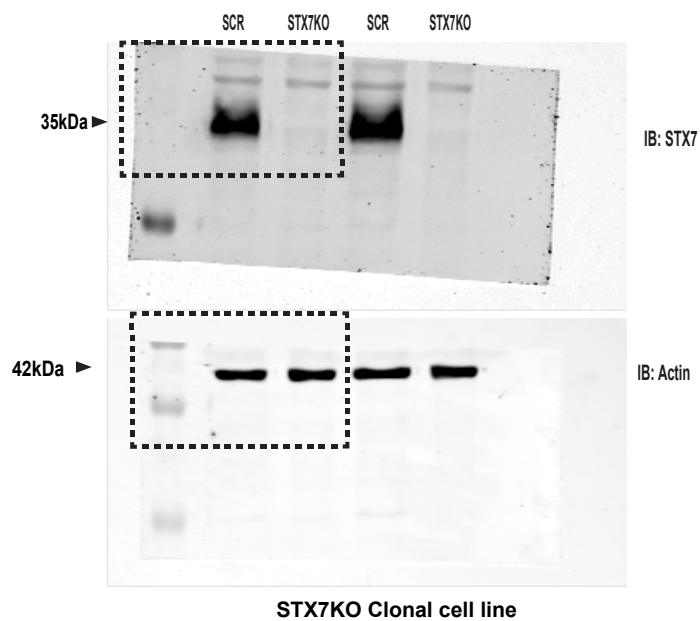


Figure 1C' (3)

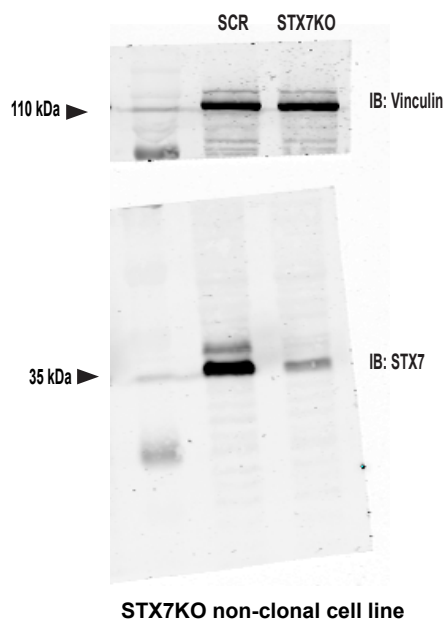


Figure 1E

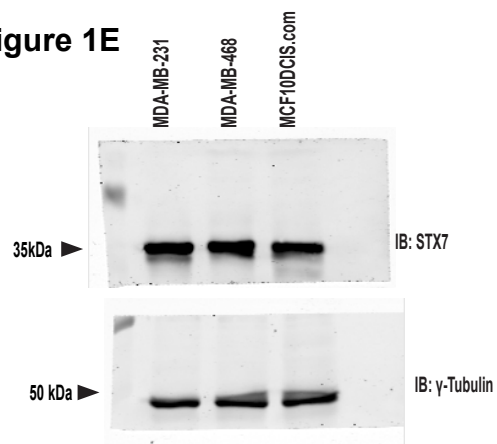
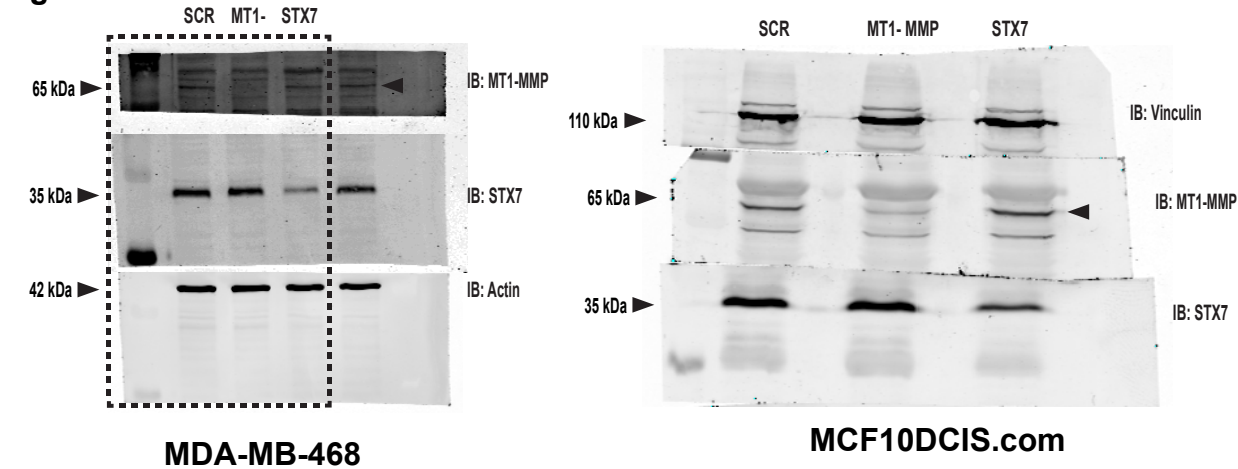
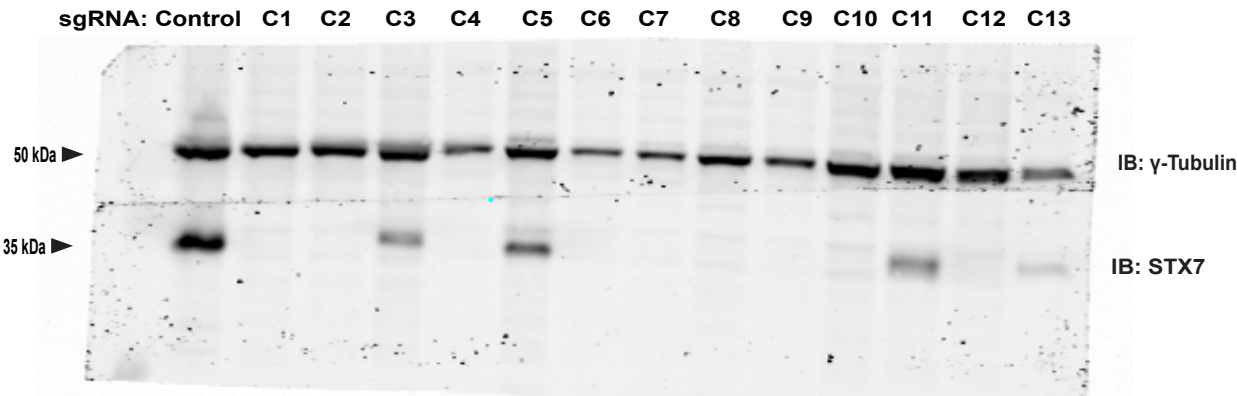


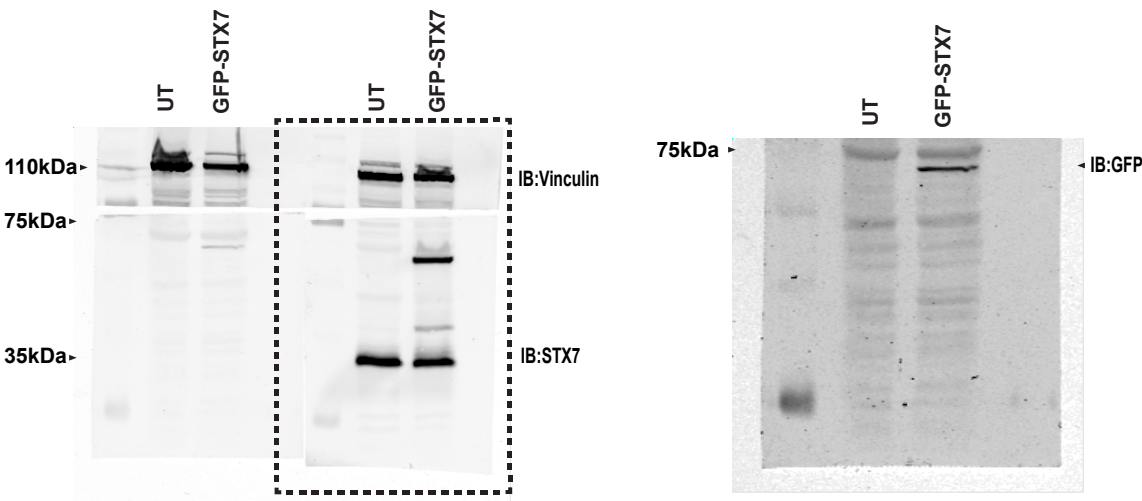
Figure 1F



Supplementary 1D



Supplementary 1E



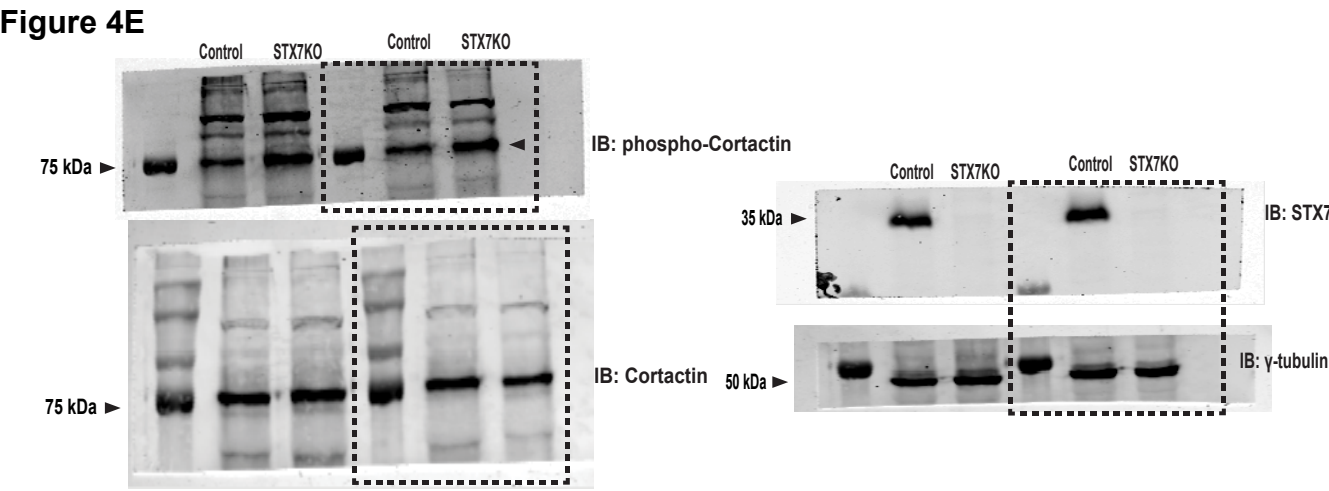
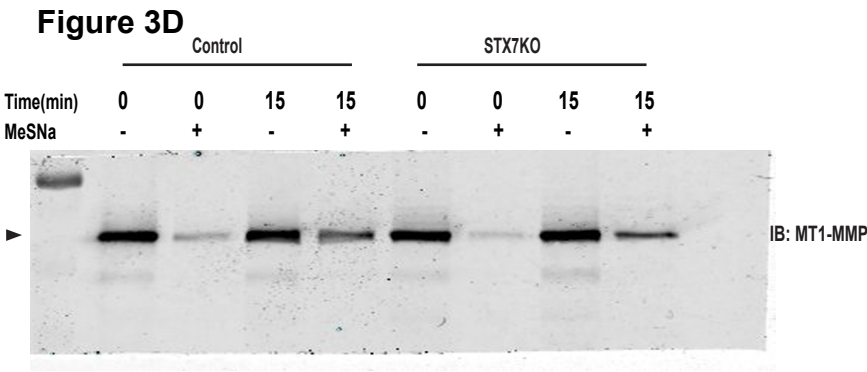
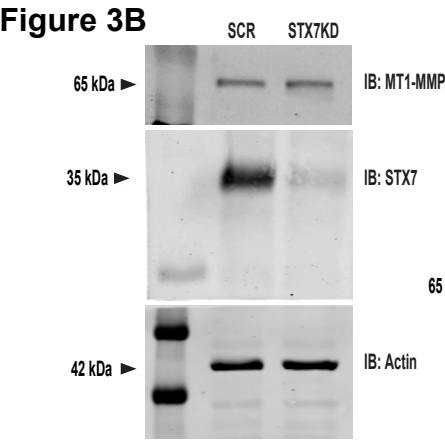
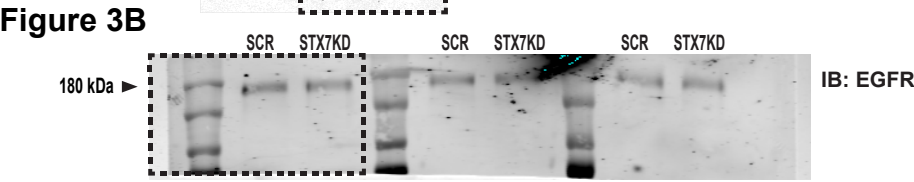
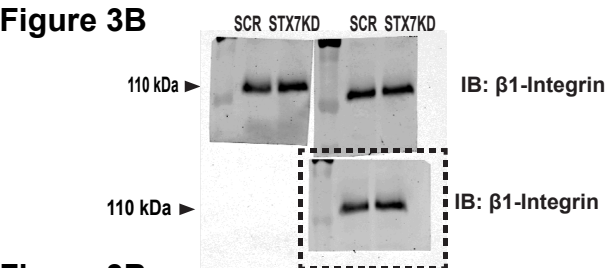
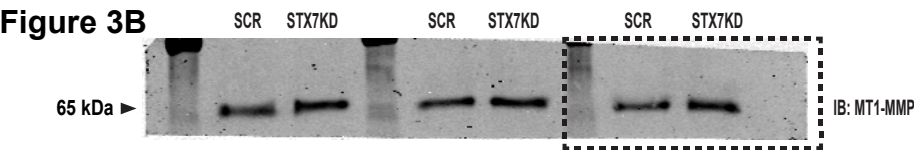


Figure 5A

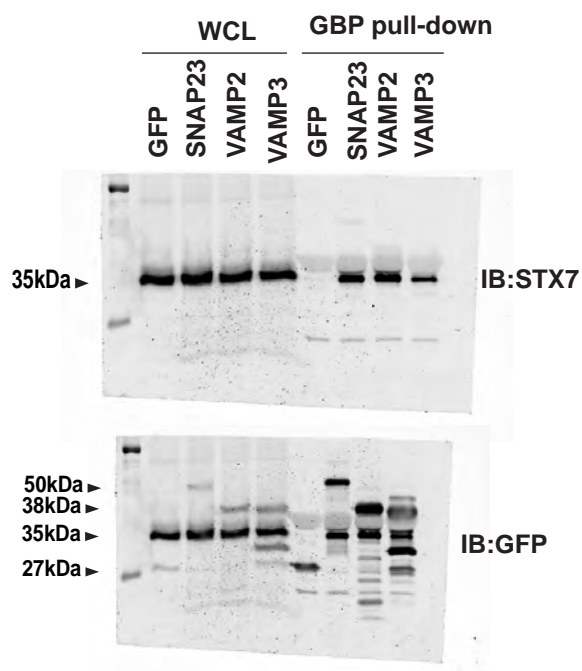


Figure 5B

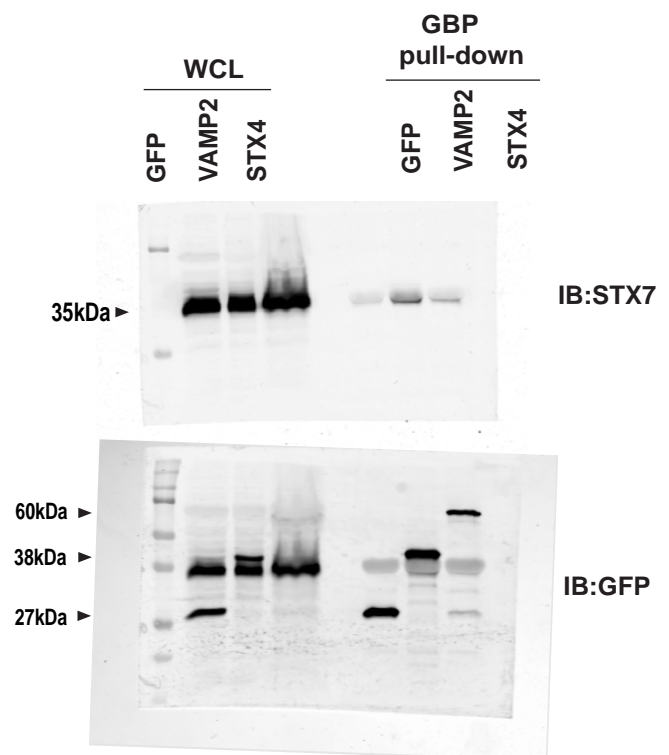
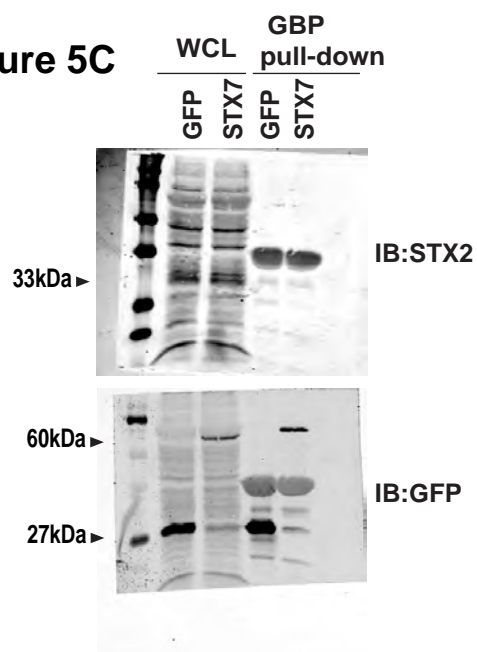
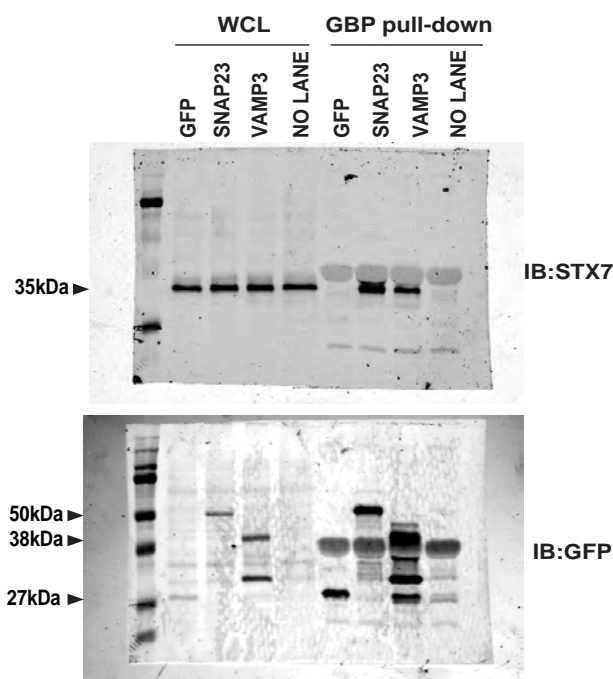


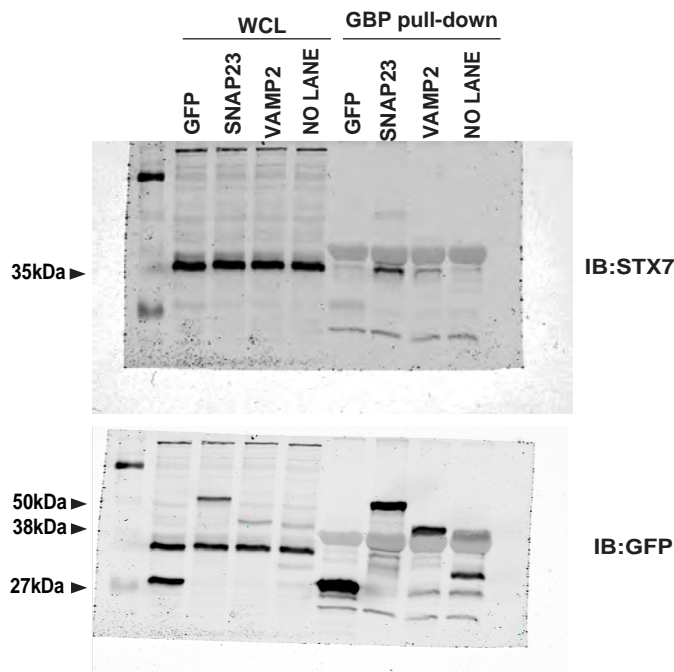
Figure 5C



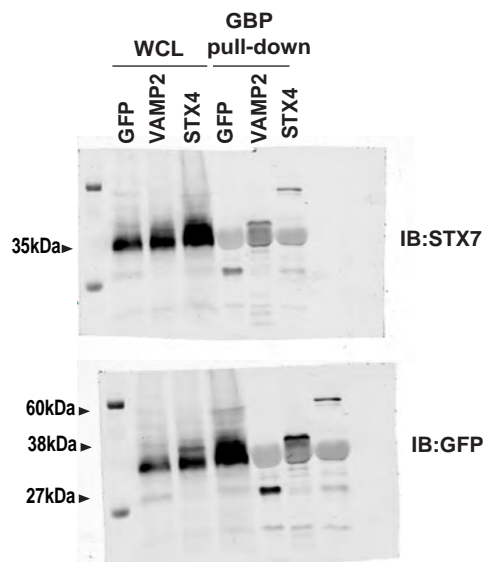
Supplementary 4A



Supplementary 4B



Supplementary 4C



Supplementary 4D

